Reviewed research article

The bedrock and tephra layer topography within the glacier filled Katla caldera, Iceland, deduced from dense RES-survey

Eyjólfur Magnússon[1], Finnur Pálsson[1], Alexander H. Jarosch[2], Tayo van Boeckel[1], Hrafnhildur Hannesdóttir[1,3] and Joaquín M. C. Belart[1,4]

[1]*Institute of Earth Sciences, University of Iceland (IES-UI), Sturlugata 7, IS-102 Reykjavík, Iceland*

[2]*ThetaFrame Solutions, Kufstein, Hörfarterstrasse 14, 6330 Kufstein, Austria*

[3]*Icelandic Meteorological Office, Bústaðavegi 7–9, 105 Reykjavík, Iceland*

[4]*National Land Survey of Iceland, Stillholti 16–18, 300 Akranes, Iceland*

Corresponding author eyjolfm@hi.is; https://doi.org/10.33799/jokull2021.71.039

Abstract — *We present results from recent low frequency radio echo-sounding (RES) campaigns over the ice-covered caldera of Katla central volcano, beneath the Mýrdalsjökull ice cap, southern Iceland. The current RES-survey both partly repeats and enhances the RES-profile grid of a previous survey in 1991 with denser sounding lines and improved instruments. The RES-data, obtained in 2012–2021, include ∼760 km of 2D migrated RES-profiles covering an area of 116 km^2. Around 14 km^2 subsections of this area were surveyed with RES-profiles 20 m apart allowing 3D migration of the RES-data. Our study confirms findings from previously published bedrock mapping, including main topographic features, ice volume stored within the 100 km^2 caldera (45±2 km^3, in autumn 2019) and maximum ice thickness (740±40 m). However, the significantly expanded level of detail and features observed in the new bedrock map reveals further evidence of a complex and eventful formation history of the caldera interior. This bedrock map is unprecedented in terms of detail for an ice-covered volcano. The new RES-data allows for a unique comparison of bedrock maps obtained from RES-data with 2D and 3D migration, demonstrating the limitations of 2D migrated RES-data in areas of high topographic variability. Reflections from the 1918 Katla eruption tephra layer within the ice were detected in a much wider area within the caldera than in the 1991 RES-data. We also observe a second internal layer at 420–580 m depth within the northern part of the caldera, identified here as the tephra from the 1755 Katla eruption. The 1918 tephra layer is typically observed at 200–300 m below the glacier surface. However, the layer depth varies from ∼100 m depth at the western rim of the caldera down to 460 m depth, where geothermal activity beneath ice cauldrons melts ice from below. At the most prominent geothermal areas all ice beneath the 1918 tephra has been melted leaving the tephra at the bed. Furthermore, the obtained tephra layer maps reveal footprints of some previously unidentified geothermal areas.*

INTRODUCTION

Many of the most active volcanoes in Iceland are ice-covered. The high elevations, found at many central volcanoes, produce an environment where more snow accumulates in winter than melts during summer, favouring glacier formation. An eruption within a glacier is usually accompanied by jökulhlaups and tephra fall (e.g. Gudmundsson *et al.*, 2008) and can be a serious threat, causing death of people and livestock and damage of agricultural land and infrastructure including houses, roads, bridges, dams, and hydropower stations. The interaction of ice and volcanism is also of broader scientific interest, with meltwater-magma interactions causing explosive fragmentation that can result in widespread airborne tephra. A sub-

glacial eruption can melt large volumes of ice and trigger powerful jökulhlaups. The Katla central volcano beneath the Mýrdalsjökull ice cap (Figure 1) is renowned for violent eruptions that are often accompanied by devastating jökulhlaups and tephra fall (e.g. Eyþórsson, 1945; Þórarinsson, 1975; Larsen, 2000, 2010; Larsen *et al.*, 2013; Óladóttir *et al.*, 2008, 2014; Smith and Haraldsson, 2005; Guðmundsson *et al.*, 2005a, 2005b, 2007, 2008, 2013; Elíasson *et al.*, 2005, 2006; Björnsson *et al.*, 2000; Tómasson, 1996; Russel *et al.*, 2010; Björnsson, 2010, 2017). Katla has also been identified as one of the largest volcanic sources of CO_2 on the planet (Ilyinskaya *et al.*, 2018).

In view of the above, Mýrdalsjökull was an obvious target for early efforts to survey and map the bedrock of Icelandic glaciers. The first attempt applied seismic reflection at nine survey sites in 1955 (Rist, 1967a), suggesting an ice thickness in the central plateau of 200–370 m. In 1977 a prototype of an analogue low frequency radar designed for use on temperate glaciers (Sverrisson *et al.*, 1980) was used to survey a few ice thickness profiles on the central plateau of Mýrdalsjökull (Björnsson, 1978). The radar system was designed to operate at frequencies low enough (3–10 MHz) to penetrate up to 1000 m thick temperate ice and reflect back enough energy from the bedrock for detection of ice thickness. In temperate ice water pockets and tunnels on various length scales up to tens of metres scatter energy from frequencies higher than tens of MHz, leaving little or no energy reflected back from the bed. An overview of the use of the low frequency radar systems to systematically map the bedrock of all major ice caps in Iceland, starting in 1978, was given by Björnsson and Pálsson (2020). The survey of Mýrdalsjökull in 1977 showed an undulating bed with 500 to 600 m thick ice in the central part and confirmed the existence of a 100 km^2 caldera below Mýrdalsjökull (Björnsson, 1978), already suggested from interpretation of Landsat images (Sigbjarnason, 1973). A distinct internal reflector at $\sim$300 m was observed and interpreted as the 1918 tephra layer. In 1991 a second RES-survey was done (Figure 2a,b), now with a fully developed version of the analogue RES-system, and Loran-C and GPS for navigation, covering most of Mýrdalsjökull, including the central part, with sounding lines at 1–2 km intervals. From this survey a topographic map (referred hereafter as a Digital Elevation Model; DEM) of both the surface and bedrock was created (Björnsson *et al.* (2000). This allowed determination of ice and water divides, estimation of the ice volume, location of the caldera rim and twelve subglacial geothermal areas, and discussion of how eruption sites relate to the bedrock topography. In the 1991 survey the internal layer seen in the 1977 profiles was visible in a large portion of the caldera, again interpreted as the 1918 tephra layer. A study of the depth of the layer suggested an average mass balance in the caldera since 1918 of 3.5–4.5 m a^{-1} water equivalent (Brandt *et al.*, 2005). The ice thickness was also surveyed at about 70 sites on Sólheimajökull (see Figure 1a for place name locations), an outlet glacier in southwest Mýrdalsjökull (MacIntosh *et al.*, 2000). The glaciology group of the Institute of Earth Science (IES) additionally conducted RES point measurements at the northeast corner of the caldera plateau (at Entujökull outlet), profiles across the K7 depression (ice cauldron, Figure 1a) that formed in 1999, and between Kötlukollar and Háabunga in 2000. An RES-profile was collected at Kötlujökull in 2003, plus 60 RES point measurements on the Kötlujökull snout in 2004 (Pálsson *et al.*, 2005).

Since 2001 the mass balance of Mýrdalsjökull has been measured in most years at a few sites in a collaborative effort of the Iceland Glaciological Society (JÖRFÍ), IES and the Icelandic Met Office (Ágústsson *et al.* 2013). The thickness of winter snow deposited in the elevation range 1300–1500 m asl on the caldera plateau is typically 10–12 m by Mid-May, corresponding to a winter balance of 5–6 m (water equivalent thickness). This is comparable to the winter accumulation measured on the 1800 m high plateau of Öræfajökull (Guðmundsson, 2000), the site where highest precipitation levels in Iceland have been measured. Ablation rates on Mýrdalsjökull (as a function of elevation) are similar to those recorded on the Breiðamerkurjökull outlet of southern Vatnajökull (Ágústsson *et al.*, 2013), resulting in an annual accumulation that typically varies between 2–5 m (water equivalent thickness) on the caldera plateau.

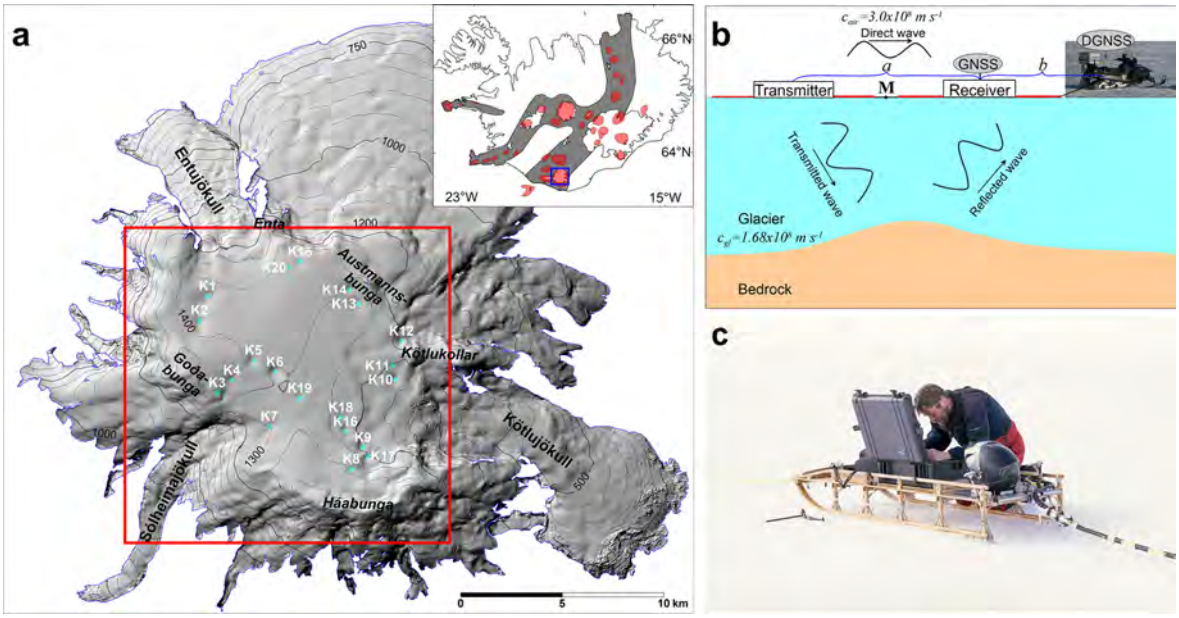

Figure 1. a) Mýrdalsjökull ice cap shown as a shaded relief image and a contour map (100 m elevation interval between contours) using a surface DEM obtained in 2010 (Jóhannesson *et al.*, 2013). This study focuses on the area within the red square. Names of outlet glaciers, glacier peaks and cauldrons are shown. Inserted map indicates the geographic location of Mýrdalsjökull (blue square) along with the neo-volcanic zones (grey) of Iceland and active central volcanoes (red). b) Schematic image showing the instruments setup for the RES-survey on Mýrdalsjökull. Red lines indicate transmitter and receiver antennae. c) The first author in the field checking the receiver unit (photograph by Þorsteinn Cameron). – *a) Mýrdalsjökull og svæðið sem hér er til skoðunar (rauður kassi) ásamt helstu örnefnum og staðsetningum sigkatla. Gráu svæðin á innfelldu myndinni sýna legu gosbeltanna og rauðu svæðin megineldstöðvar. b) Skýringarmynd af uppsetningu íssjármælibúnaðar. c) Fyrsti höfundur greinar að athuga íssjármóttakara (myndina tók Þorsteinn Cameron).*

Jökulhlaups originating in Mýrdalsjökull are frequently observed on rivers flowing from the ice cap. The largest of these have been caused by eruptions in Katla; the peak flow of the jökulhlaup in 1918 has been estimated at ∼300,000 m^3 s^{-1} (Tómasson, 1996). Most of the jökulhlaups are, however, known to originate from the geothermal areas at the glacier bed. The geothermal areas typically form and maintain circular or semi-circular dips in the glacier surface, generally referred to as ice cauldrons (e.g. Björnsson, 1975); 20 of them have been denoted with the names K1 to K20 (Figure 1a). Beneath some of these cauldrons, water can collect and subsequently be released in jökulhlaups, resulting in lowering of the cauldron surface. Jökulhlaups originating from beneath these cauldrons are of variable magnitude with peak drainage between a few m^3s^{-1} to a few thousand m^3s^{-1}. The surface elevation of the ice cauldrons has been monitored by means of radar altimetry or ground Differential Global Navigation Satellite System (DGNSS) profiling since 1999 (Gudmundsson *et al.*, 2007; Gudmundsson and Högnadóttir, 1999–2020).

The three best known jökulhlaups since the 1918 eruption, all with a peak discharge that probably exceeded 1000 m^3s^{-1} (Larsen *et al.*, 2013), occurred in Múlakvísl and Skálm, 25 June 1955 (Rist and Þórarinsson, 1955; Thorarinsson, 1957; Rist, 1967b; Tryggvason, 1960), destroying bridges over both rivers; in Jökulsá á Sólheimasandi, 18 July 1999 (Sigurðsson *et al.*, 2000; Guðmundsson *et al.*, 2007), cutting the power line across Sólheimasandur outwash

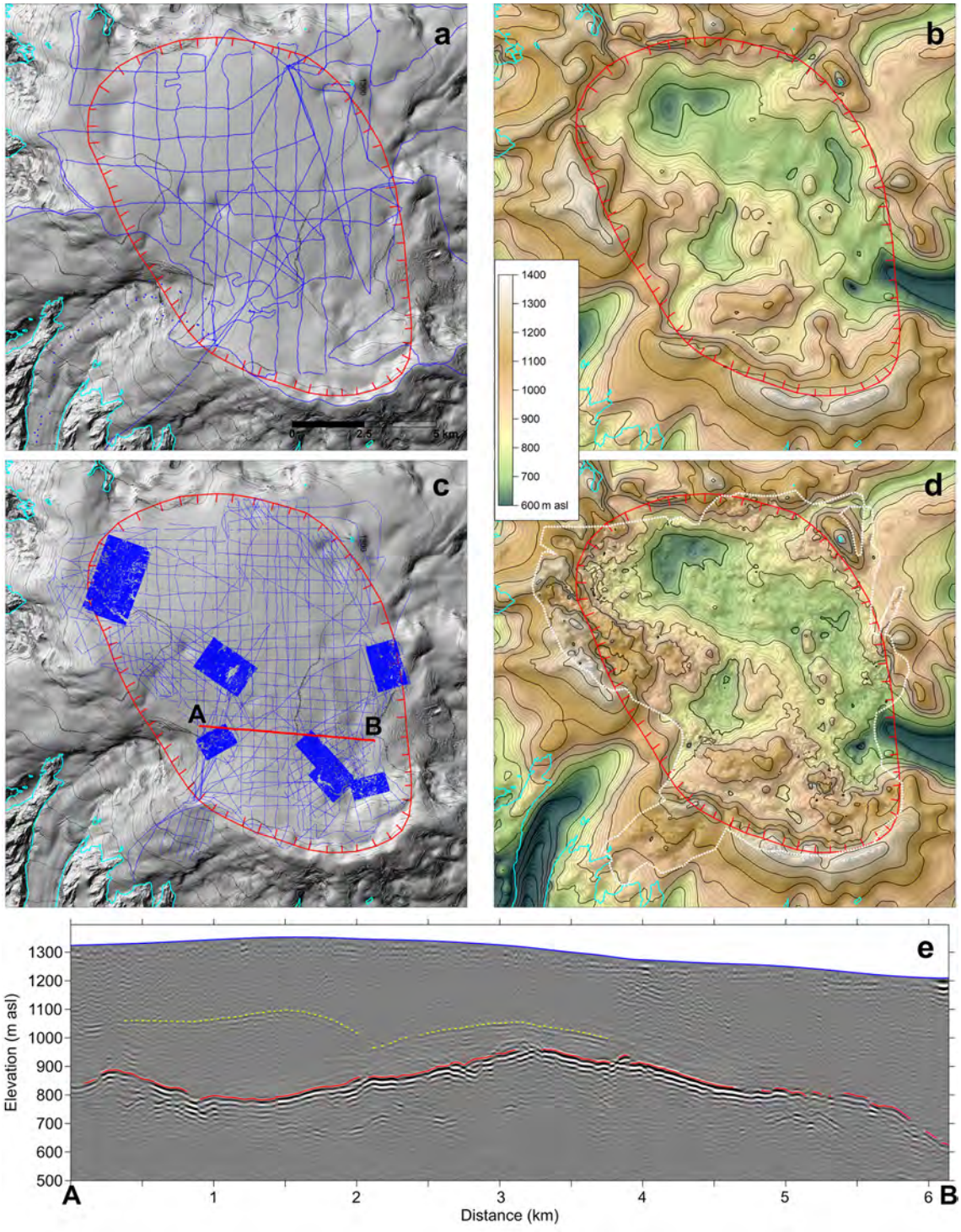
a
b
c
d
e
0
2.5
5 km
1400
1300
1200
1100
1000
900
800
700
600 m asl
A
B
Elevation (m asl)
1300
1200
1100
1000
900
800
700
600
500
1
2
3
4
5
6
Distance (km)

plane and threatening the bridge across the river, and Múlakvísl, 9 July 2011, washing away the bridge over the river (Guðmundsson and Högnadóttir, 2011; Jónsson and Þórarinsdóttir, 2011; Jóhannesson, 2012). These jökulhlaups are all thought to have been associated with sudden energy release at the bed, from shallow magmatic intrusions within the bedrock, due to minor subglacial eruptions or via hydrothermal processes. Gudmundsson *et al.* (2007) associated the 1999 event with a small eruption at the glacier base given the short estimated time of melting at the bed (hours or days). Chemical analysis, however, indicated that magma had not been in direct contact with the glacier ice or the subglacial water released in the 2011 event (Galeczka *et al.* 2014). Study on the related seismicity (Sgattoni *et al.*, 2019) was, however, not conclusive in regard to whether magmatic or hydrothermal processes produced the melt released during these three events.

The jökulhlaups in 1955, 1999 and 2011 were sudden and unforeseen. Following the 2011 jökulhlaup, attempts were made to monitor the cauldrons by surveying RES-profiles with low frequency radar (5 MHz) to look for signs of water accumulation. This was done simultaneously with the ground DGNSS surface elevation profiling. RES-profiling across the Mýrdalsjökull cauldrons has continued, following the same track as accurately as possible, once or twice every year since May 2012 looking for signs of significant water accumulation as temporally elevated reflections beneath the cauldrons (Magnússon *et al.*, 2017). Similar RES-monitoring has also been successfully adopted for the Eastern Skaftá cauldron in Western Vatnajökull since 2014 (Magnússon *et al.*, 2021). In 2016, the monitoring on Mýrdalsjökull initiated with a support from the Icelandic Road Administration Research Fund, developed into the research project Katla Kalda, supported by Rannís via the Icelandic Research Fund. The basic objective of the Katla Kalda project is to improve understanding of the collection and drainage of water from subglacial geothermal areas. To achieve this, the repeated RES-survey, initiated in 2012, was continued and expanded. High resolution (sub-meter) optical satellite images (Pléiades) have been repeatedly acquired for the purpose of producing surface DEMs and detecting surface elevation changes within the cauldrons. Surface changes of Mýrdalsjökull in the past decades have also been studied (Belart *et al.*, 2020). Continuously recording GNSS instruments were deployed in various ice cauldrons to obtain records of jökulhlaup timing, duration and surface subsidence. Conductivity variation in the rivers draining these jökulhlaups was also studied (Einarsson, 2019). An automatic weather station (to estimate the surface energy balance) has been operated during summers and information on surface melting as well as motion has been obtained by deploying mass balance stakes in and around ice cauldrons in spring and revisiting them in the autumn. Finally, high

Figure 2. a) The location of RES-data used in the pre-existing bedrock DEM (b) of our study area (Björnsson *et al.*, 2000, with further unpublished improvements, by the IES-glaciology group, for limited area based RES-profile and point survey in 2000–2003). c) The location of RES-data used to create the new bedrock DEM (d) presented here. The white dotted line in d) indicates which part of the bedrock DEM is revised here. The background shaded relief images in a and c show the glacier surface in 2010 (Jóhannesson *et al.*, 2013) and the red hachured polygon indicates the rim of the Katla caldera (Björnsson *et al.*, 2000). The cyan lines in a–d show glacier margin and nunataks in 2010. e) An example of a 2D migrated RES-profile, measured in 2016, from A to B (locations shown in c). Red lines indicate traced bedrock, yellow dotted lines the traced 1918 tephra layer. *– a) Lega íssjármælilína (að mestu mældar 1991) sem eldra botnkort (b) byggir á. c) Lega mælilína til grundvallar þess korts sem hér er birt (d). Svæðið utan hvítu punktalínunnar er óbreytt frá eldra korti. Myndir a og c sýna yfirborð jökulssins (skuggamynd og hæðarlínur) og útmörk (blágrænar línur) sumarið 2010. Rauð hökuð lína á a–d, sýnir brún Kötluöskjunnar. e) Dæmi um íssjársnið með tvívíðri staðsetningarleiðréttingu endurkastsflata (e. migration), mælt vorið 2016 frá A til B (staðsetning sýnd á c). Rauðar línur sýna rakin botnendurköst en gula punktalínan endurköst frá gjóskulaginu sem féll á jökulinn í gosinu 1918.*

emphasis has been placed on improving the bedrock topography map of the caldera, with specific focus on the ice cauldrons and their vicinity. In this paper we present results from RES-field campaigns, carried out in 2016–2021 on Mýrdalsjökull for this purpose, as well as some pre-existing RES-data dating back to 2012. The outcome is a new bedrock DEM based on much denser observations than in 1991 (Figure 2a–d). The DEM is particularly elaborate around many of the ice cauldrons where RES-profiles only 20 m apart were surveyed, allowing for 3D migration of the reflections (e.g. Moran *et al.*, 2000), greatly enhancing details and accuracy of the bedrock topography. The new RES-data was also used to map ice thickness above the 1918 tephra layer as well as the ice thickness above a tephra layer detected in the northern part of the caldera and linked here with the 1755 eruption of Katla using a full Stokes ice flow model. We discuss the subglacial topographic features revealed in this study, and imprints of geothermal activity seen in the topography of the tephra layers, including evidence for previously unknown activity. Finally, we discuss the possibility of further studies enabled by the presented data sets.

DATA AND METHODS

RES-data

The RES-data used in this study were acquired in 2012–2021 and cover 116 km^2, mostly within the glacier-filled caldera of Katla central volcano in Mýrdalsjökull (Figures 2c and 3). The RES-data allows construction of a detailed bedrock elevation DEM and maps of ice thickness above two isochrone layers marked by tephra fall on the glacier surface during eruptions. The RES-data set includes approximately 760 km of 2D migrated RES-profiles, which partly repeats the survey of 1991 in this area (Figure 2a) but enhances the network with denser profiles. Most of the area has been surveyed with north-south and east-west profiles, where distance between profiles is typically 400–500 m for both directions. For the cauldron areas, profiles ∼200 m apart were surveyed

Figure 3. The data used for interpolating the new bedrock DEM. Blue lines indicate location of traced bedrock reflections from 2D migrated RES-profiles used directly without modification. Red lines indicate location of traced bed reflections in the 2D migrated profiles considered as cross track reflection and therefore, either omitted or shifted cross track (yellow lines) to fit bedrock elevation from crossing RES-profile. Magenta clusters indicate location of traced bed reflections from 3D migrated RES-data (Table 1) tagged with names of survey areas (mostly cauldron names). The area outside the white dotted polygon, covered with transparent grey mask indicates bedrock DEM not modified in this study. The elevation of the previous bedrock DEM at the border (white dotted line) was used as additional input to the interpolation to secure smooth mosaic of the new and the unchanged previous DEMs. The elevation at glacier margin and nunataks boundary (cyan line) within the white dotted polygon were also added as input in the bedrock interpolation. Purple lines indicate manually digitized elevation contours added in areas where interpolation without any further constraints resulted in odd topographic features. – *Gögn sem eru notuð til að brúa nýtt botnhæðarkort. Bláar línur sýna staðsetningar botnendurkasta úr íssjársniðum, sem unnin eru með tvívíðri staðsetningarleiðréttingu á endurkastsflötum og notuð við brúun botnhæðarkorts án frekari leiðréttinga. Rauðar línur sýna endurköst úr samskonar sniðum sem talin voru vera hliðarendurköst og því annað hvort sleppt í brúunarreikningum eða hnikað til hliðar (gular línur) þannig að botnhæðir falli að mælingum úr sniðum sem liggja þvert yfir viðkomandi íssjársnið. Purpurarauðar skellur, merktar með nafni mælisvæðis (aðallega nöfn katla), sýna staðsetningar botnendurkasta úr íssjársniðum, unnar með þrívíðri staðsetningarleiðréttingu á endurkastsflötum (1. tafla). Hæðum úr eldra botnhæðarkorti á hvítu punktalínunni var bætt við sem inntaksgögnum í brúunina til að tryggja samfellu við það svæði sem er óbreytt frá eldra korti (gráskyggða svæðið utan hvítu punktalínunnar). Einnig voru landhæðir við jökuljaðar og á útmörkum jökulskerja (innan hvítu punktalínunnar) nýttar við brúun nýja botnkortsins. Fjólubláar línur sýna handteiknaðar hæðarlínur sem bætt var við brúunargögnin á svæðum þar sem brúun án frekari skorða skilaði ónáttúrulegu botnlandslagi.*

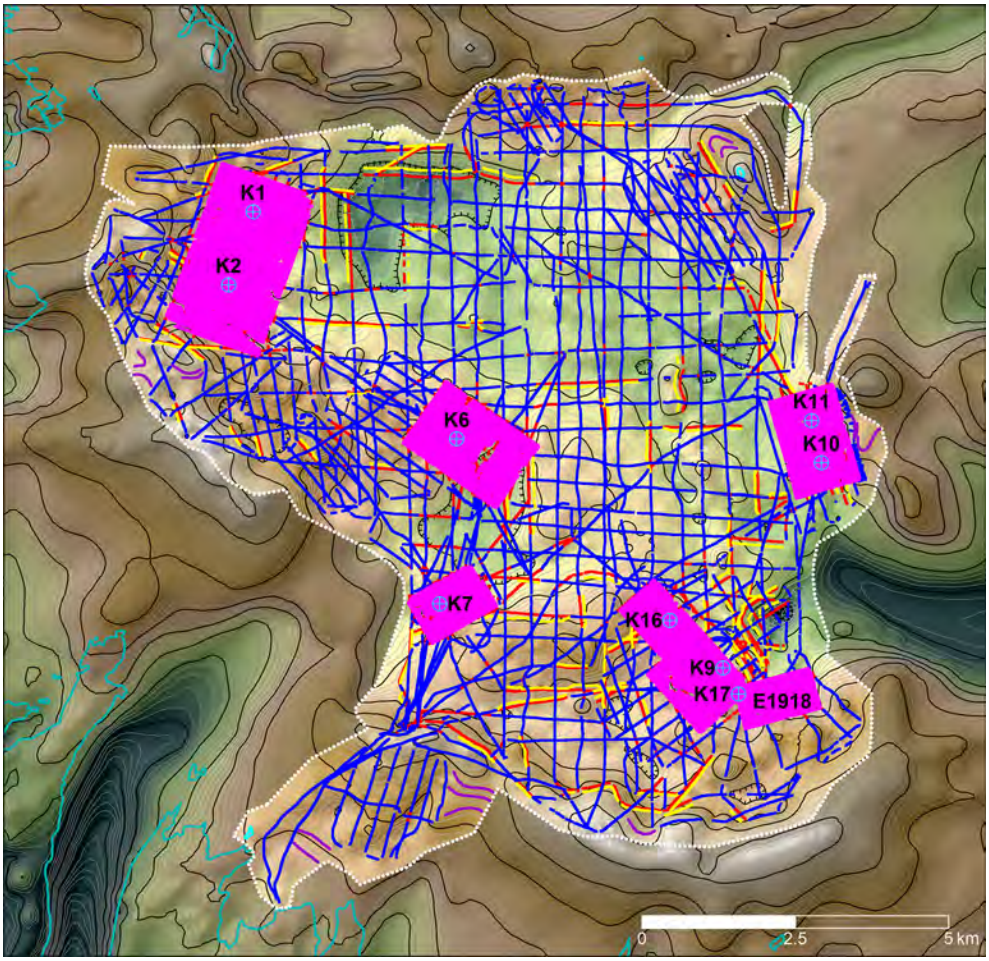

approximately along the overall surface slope direction of each cauldron area. Most of the 2D migrated RES-profiles were surveyed on 14–19 May 2016, 2 February 2017, 19 May 2019 and 15 May 2021. Other 2D migrated data used includes RES-profiles that have been repeatedly surveyed across many of the cauldrons since spring 2012, with the aim to detect if substantial water accumulation were occurring beneath the cauldrons (Magnússon *et al.*, 2017).

A far more detailed survey was carried out for several of the cauldron areas and the estimated location of the 1918 eruption (Guðmundsson *et al.*, 2021), where profiles with 20 m interval were surveyed (Figure 4a), enabling 3D migration of the survey data. Such data sets are not commonly acquired from glaciers, even though several studies applying this survey approach have been reported (e.g. Moran *et al.*, 2000; Schlegel *et al.*, 2020). This approach was adopted for several subsections of our survey area (total of 14 km^2, Figure 3), with most surveyed more than once. K1, K2, K6 and K7 and their vicinity were surveyed twice, and K10, K11 and K16 five times (Table 1). Only a single survey was carried out at K9, K17 and the estimated location of 1918 eruption (survey area labelled E1918 in Figure 3). The focus of the repeated survey was to study changes in location of bed reflections related to water accumulation and depletion beneath the cauldrons (Figure 4d,e). This subject is, however, mostly beyond the scope of the current paper.

Table 1. List of 3D migrated RES-data sets with corresponding observation dates and locations. The 1918 tephra layer was traced from the data sets marked with T. The traced bed reflection from data sets marked as slave data sets (S) are correct by comparison with master data sets (M) as described in main text. The letter U indicates that no such correction was carried out. In such cases most of the traced reflections originate from the data set marked with *. The other data sets were only partly traced but used to fill data gaps, e.g. in areas subglacial water chambers likely covered the bedrock when the * marked data set was surveyed. *– Listi yfir íssjármælingar sem unnið var úr með þrívíðri staðsetningarleiðréttingu á endurkastsflötum ásamt tíma og staðsetningum. Mælingarnar merktar með T (e. tephra) voru nýttar til að rekja gjóskulagið frá 1918. Hæð greindra botnendurkasta í S (e. slave) merktum gagnasettum hefur verið leiðrétt með samanburði við gagnasett merkt M (e. master). Engin leiðrétting hefur verið gerð á svæðum þar sem gagnasett er merkt með U (e. uncorrected) en í þeim tilfellum voru gögnin sem nýttust við gerð botnkortsins að mestu úr stjörnumerktum mælingum en hin gagnasöfnin einungis nýtt til að fylla í eyður, t.d. þar sem vatnsgeymar skyggja á botn í stjörnumerktu íssjármælingunum.*

Date / Cauldron	K1 & K2	K6	K7	K9 & K17	K10 & K11	K16	E1918
May 2013					S		
May 2014					S		
May 2017		S T	M T		U T	S T	
October 2017		M T	S		S		
March 2018					U		
May 2018	U*				U		
November 2018	U T				U		
May 2019				U	U*	M	
May 2021							U

Figure 4. a) The location of planned (black) and actual (green and red) RES-survey profiles for 3D migration obtained in May and October 2017 at K6. b,c) Locations of traced bed (b) and tephra layer (c) reflections from the two data sets. d–i) Examples of 3D migrated profiles along (d–f, from A to B, locations shown in a–c) and perpendicular (g–i, from C to D, locations shown in a–c) to the direction of the survey profiles. Traced reflections from bedrock, tephra and roof of water bodies are shown. Reflections from the bed were masked out before the 3D migration of profiles f and i (see Data and Methods for further details). Profile (i) is a mosaic of results from spring and autumn 2017. All profiles (d–i) are without vertical exaggeration. *– a) Útsett mæliplan (svartar línur) og mæld íssjársnið í maí (græn) og október (rauð) 2017 yfir katli 6, sem unnin voru með þrívíðri staðsetningarleiðréttingu á endurkastsflötum. b,c) Staðsetning endurkasta frá föstum jökulbotni (b) og 1918 gjóskulaginu (c) sem greind voru í þessum íssjársniðum. d–i) Dæmi um íssjársnið, unnin með þrívíðri staðsetningarleiðréttingu, samsíða (d–f, lega sniðs frá A til B sýnd á a–c) og hornrétt á (g–i, lega sniðs frá C til D sýnd á a–c) útsett mælisnið. Punktalínur sýna rakin endurköst frá föstum jökulbotni (purpurarauð), gjóskulagi (gul) og þaki vatnsgeymis (blágræn). Endurköstum frá föstum jökulbotni var eytt út fyrir þrívíða staðsetningarleiðréttingu á endurkastsflötum í (f) og (i) en sú síðarnefnda er samsett úr mælingum frá vori og hausti 2017. Íssjársnið (d–i) eru án hæðarýkingar.*

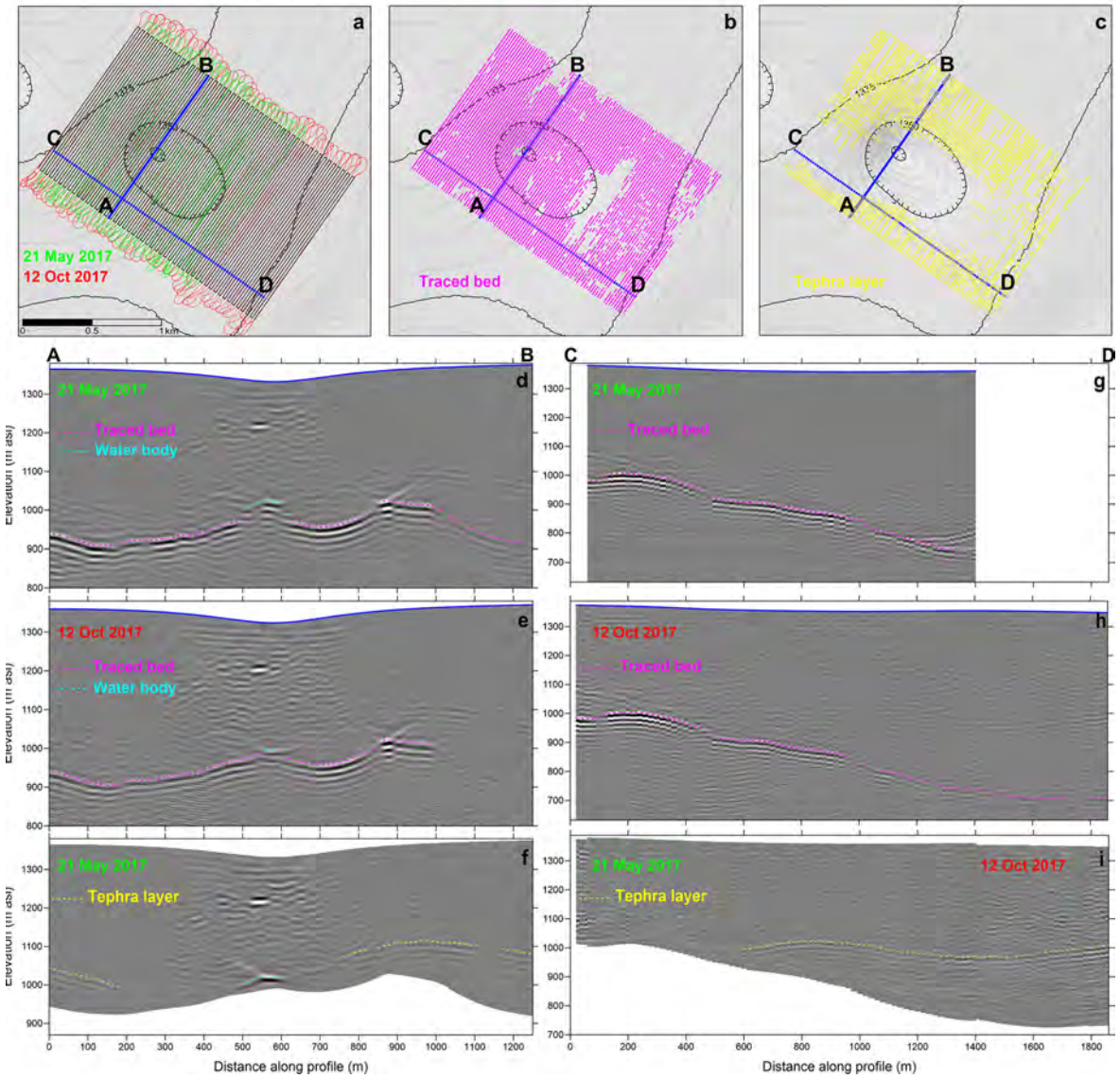

The RES processing closely follows Magnússon *et al.*, (2016) for 2D migrated data and Magnússon *et al.* (2017) for 3D migrated data. The RES-data were acquired by towing a low frequency transmitter (5 MHz centre frequency) and a receiver unit on sledges, separated by distance, *a*, varying from 30 to 40 m, with corresponding antennae in a single line on a snowmobile, equipped with a DGNSS receiver (Figure 1b). The receiver unit as well as the transmitter used before 2016, in 2017 and partly in 2018 was developed by Blue System Integration Ltd. (see Mingo and Flowers, 2010). The transmitter used in 2016 and again in 2018 and later was developed by Sverrisson *et al.* (1980). The raw RES-data (series of amplitude/time records) are processed as backscatter images where the x-axis corresponds to the number of the RES-survey records (each record consists of 256 or 512 stacked measurements). The y-axis

is the travel time of received backscattered transmission relative to the triggering time of the measurement; the receiver measurement is triggered by the direct wave propagating along the surface from the transmitter (Figure 1b). The centre position, **M**, between transmitter and receiver for each RES-survey was obtained using the GNSS timestamp obtained by the receiver unit for each RES-survey, and the corresponding position of the DGNSS on the snowmobile projected back along the DGNSS profile by a fixed distance (Figure 1b). This distance corresponds to the half the antenna separation (a/2) plus the measured distance b, from the RES-receiver sledge to the snowmobile (location of the DGNSS antennae). b was 20–22 m in the surveys described here. Except when taking sharp turns, the horizontal accuracy of **M** is expected to be < 3 m. Errors are mainly due to variation in distance to the snowmobile, inexact timing of each RES-survey (the survey plus processing time of the stacked measurements varies slightly but is typically $\sim$1 s), and inaccuracy in how well the towed sledges follow the snowmobile path. The vertical accuracy in surface elevation measured with the DGNSS, is typically a few decimetres. The strong direct waveform is estimated as the average wave form measured over several km long RES-profile segments and then subtracted from the corresponding segment of the raw RES-measurements. The remaining part of the measured backscatter, mostly from englacial and subglacial reflectors, was amplified as a function of the travel time in order to have the backscatter strength as independent as possible of the reflector depth. The next processing steps depend on whether 2D or 3D migration was applied.

2D migrated RES-data

In case of 2D migration, the amplified RES-data along with the 3D location, **M**, for each measurement and corresponding transmitter and receiver 3D positions (a/2, behind and in front of **M**, respectively, along the DGNSS profile) were used as inputs into a 2D Kirchhoff migration (e.g. Schneider, 1978), programmed in MATLAB(®Mathworks). The migration was carried out assuming propagation velocity of the radar signal through the glacier, c_{gl}=1.68$\times$ 10^8 m s^{-1} and 500 m width of the radar beam illuminating the glacier bed. The value of c_{gl} is the same as obtained by comparison of a borehole survey and RES-data in the eastern Skaftár cauldron located in the accumulation area of Vatnajökull (Magnússon *et al.*, 2021) and only slightly lower than the value used in previous mapping of Mýrdalsjökull by Björnsson *et al.*, (2000), which used the value c_{gl}=1.69$\times 10^8$ m s^{-1}. The 2D migration results in profile images like the ones shown in Figure 2e. The x- and y-axis of these images correspond to driven profile length and elevation in metres above sea level, respectively. The image pixel dimensions, dx=5 m and dy=1 m, roughly correspond to the horizontal sampling density when measuring with $\sim$1 s interval at $\sim$20 km hour^{-1}, and the 80 MHz vertical sampling rate (in 2012–2017 and in 2021; it is 120 MHz for a new receiver unit used in 2018–2019).

Backscatter from the glacier bed is usually recognised as the strongest continuous reflections at depth in the 2D migrated amplitude images. They were traced with an automatic tracing algorithm, programmed in MATLAB (®Mathworks). The algorithm traces the bed reflection by using the maximum correlation with the bed reflection at the chosen starting point. The obtained traces were manually checked and rejected where the algorithm failed. This process was repeated until all clear bed reflections had been traced for each profile of an individual survey. At sharp turns in the survey profiles reflections were rejected. The assumption of fixed distance between transmitter and receiver fails at these turns and the 2D migration is not expected to result in an accurate depth of reflector.

3D migrated RES-data

The input into the first specific processing step of the 3D migration is the RES-data, amplified as function of the travel time, acquired for a dense set of parallel profiles, 20 m apart (Figure 4a). The surveys were carried out by manually following a pre-planned route in the navigation instrument of the snowmobile. The survey point positions (**M**) deviate slightly from the pre-planned route (Figure 4a). At this stage a 3D matrix (a cube) was linearly interpolated from the survey data, with first axis in the direction of the planned survey tracks (5 m node interval) and second axis in cross track direction (10 m node interval). The third axis of

the cube is the travel time of the reflected radar wave, with time interval corresponding to double sampling frequency ($0.625\times\ 10^{-9}$ s for data acquired with 80 MHz sampling frequency in 2013 to spring 2017 and 2021 and $0.4167\times\ 10^{-9}$ s for data acquired with a new receiver recording at 120 MHz from autumn 2017 to 2019). The interpolated cube also covered a 50 m wide area on each side of the cube corresponding to the area just before and after turning the snowmobile 180° to measure a new line (Figure 4a). The interpolated cube mimics the RES-survey point matrix at the surface with positions (**M**) corresponding to the exact column locations of the cube with the receiver and transmitting antenna placed along the first axis of the cube at distance $A/2$ behind and in front of **M**. Therefore, all survey points where the driving direction deviates more than 10° from the profile direction were omitted before the interpolation. If the input data at a given position near the edge of the cube were insufficient for linear interpolation, the corresponding column was left with zero values.

Next a 3D Kirchoff migration (e.g. Schneider, 1978) was applied on the regularly interpolated cube, using c_{gl}=1.68$\times\ 10^8$ m s^{-1} and 250 m search radius. Additional input required for the migration are the positions and elevations for each interpolated radar-shot in the cube for the receiver and transmitter; the elevation values were extracted from a surface DEM interpolated from the simultaneous DGNSS survey. The output yields a set of profile images identical to the ones obtained with 2D migration in terms of axis definition (x=distance, y=elevation) and pixel dimension (dx=5 m, dy=1 m). The output profiles correspond to those in the pre-planned survey route (20 m apart), excluding the profiles at the edges. At the edges of the area spanning the migrated profiles the search radius extended outside the input data. To compensate for this, the migrated output data was scaled by the reciprocal of the number of input survey points from the interpolated cube.

When tracing reflections in the 3D migrated data (Figure 4) the same approach was adopted as for the 2D migrated data, using each migrated profile obtained in the track direction. The tracing results were also revised by comparing cross track images extracted from the 3D migration with the posted tracing (Figure 4g–i). Sometimes further tracing was conducted from cross track profiles. A systematic elevation difference was sometimes observed between traced bed reflections of different surveys (typically 1–3 m), attributed to different transmitters used, inaccuracies in tracing, or temporal changes in the propagation velocity of the radar wave. To minimise topographic artefacts, which may arise when data from different times are used, a master data set was defined (Table 1). The median difference between the elevation of traced reflections from master and individual slave data set at fixed locations was calculated for sub-sections of three neighbouring along-track profiles and used as correction for the corresponding slave profiles. After applying such correction, where needed, the lowermost trace was considered as the bedrock elevation and other traces omitted. Traced reflections significantly above the assumed bed elevation (based on all available data) were likely reflections from the top of subglacial water bodies (Figure 4d–e). At a few locations, the traced reflections were considered to be from water bodies for all surveys, hence the corresponding location was left without traced bedrock (e.g. common location of cyan lines in Figure 4d–e).

The bedrock traces from 3D migrations were at this point exported as a list of coordinates, x,y,z, (easting and northing in ISN93 Lambert projection (EPSG code 3057, National Land Survey of Iceland) and bedrock elevation in metres above sea level (ISH2004, National Land Survey of Iceland)) and used without further revision as input into interpolation of the bedrock DEM (Figure 3).

Revision of bedrock data and construction of bedrock DEM

The traced reflections of the 2D migrated data were filtered with a 25 m wide triangular filter and downsampled at 20 m interval along the profile (Magnússon *et al.*, 2016) prior to extracting a coordinates list identical to the one obtained from the 3D migrated data (see above). All points derived from the 2D migrated data, located within the areas of 3D migrated data, were omitted. Cross-point mismatches with bedrock elevation difference of 5 m or higher,

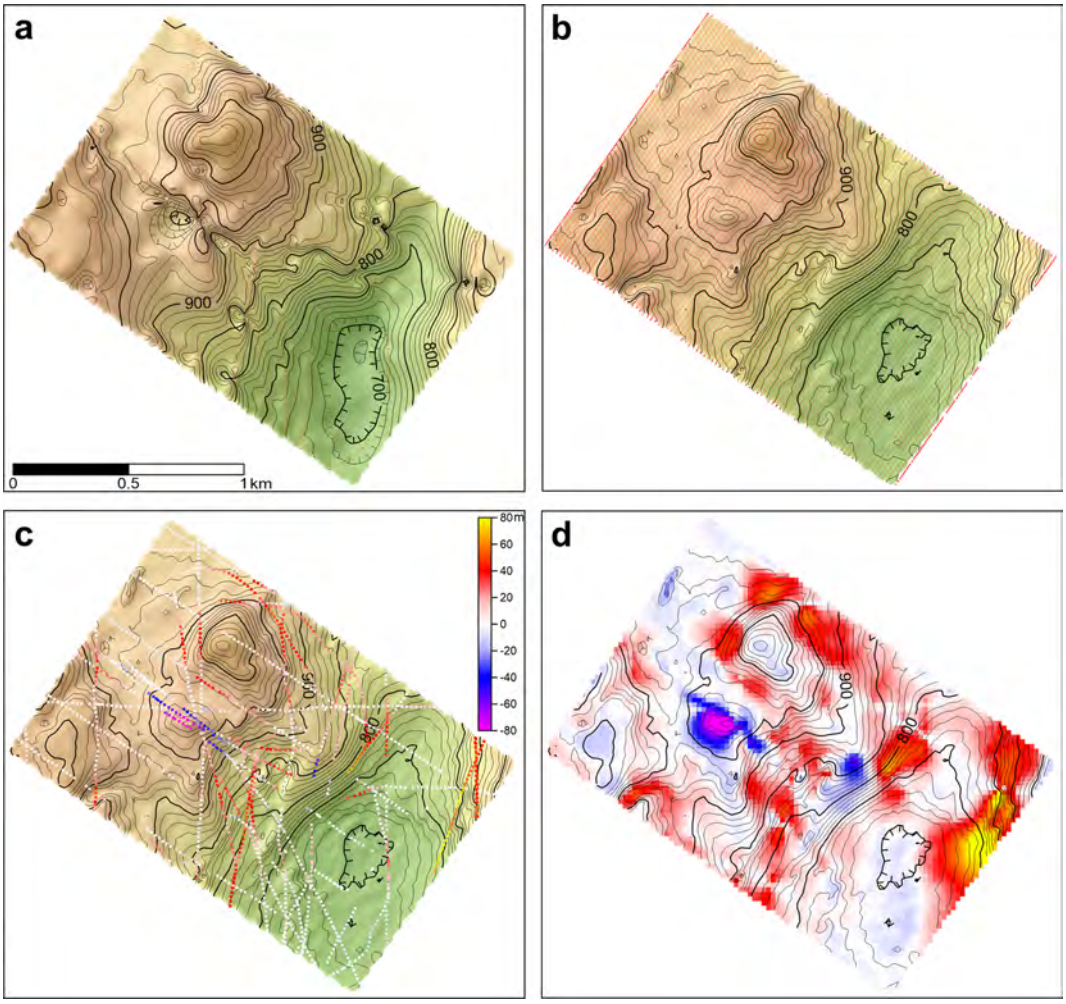

Figure 5. a,b) The interpolated bedrock DEMs based on 2D (a) and 3D (b) migrated RES-data at K6 shown as contour maps (10 m contour interval) overlain with the locations of traced reflections (transparent red points) from corresponding data set. The DEM shown in b is also shown as contours on (c) and (d). c) The difference between the bedrock DEM obtained from 3D migrated data and elevation of the traced bed reflection in the 2D migrated profiles. d) The difference between the DEMs shown in a and b. Positive values (represented with warm colours) indicates 2D migrated bedrock higher than 3D migrated bedrock. – *a,b) Hæðarkort (10 m hæðarlínubil) af föstum jökulbotni brúað út frá hæð botnendurkasta sem greind voru í íssjársniðum unnum með tvívíðri (a) og þrívíðri (b) staðsetningarleiðréttingu á endurkastsflötum, botnhæðarkort á mynd (b) er einnig sýnt á myndum (c) og (d). Kortin ná yfir ketil 6 og næsta nágrenni. Rauðir punktar sem felldir eru ofan á kortin sýna staðsetningu botnhæðargagnanna sem voru brúuð. c) Mismunur botnhæðarkorts sem unnið er með þrívíðri staðsetningarleiðréttingu og botnhæðar úr íssjársniðum með tvívíðri staðsetningarleiðréttingu á endurkastsflötum. d) Mismunur botnhæðarkorta (a) og (b). Jákvæð gildi (sýnd með heitum litum) gefur til kynna að botn fenginn með tvívíðri staðsetningarleiðréttingu standi hærra en sá sem fæst með þrívíðri staðsetningarleiðréttingu.*

were reviewed. Most observed mismatch was due to the limitation of the 2D migrated RES-profiles. When profiles are not driven parallel to the maximum slope of a steep bed, the traced bed reflection may originate from cross-track bed reflections up-slope from the measurement location, hence the obtained bed reflections appear higher than the actual bed directly beneath the profile (e.g. Lapazaran *et al.*, 2016). This is clearly demonstrated by comparison between traced reflections from 2D and 3D migrated RES-profiles around K6 (Figure 5). At locations where this explained the mismatch, the profile more closely matching the bed slope direction was kept unchanged while the data from the crossing profiles was either omitted or shifted between 5 m and 130 m cross track in up slope direction to fit the bed elevation of the crossing profile (Figure 3). In the few cases where neither profile followed the bed slope direction, both profiles where shifted (< 50 m) cross-track to obtain a match at the crossing point. At a few locations where the mismatch could not be related to the shortcoming of the 2D migrated RES-profiles, the bed-tracing was revised. This usually revealed discrepancy in the interpreted bed reflections for the crossing profiles. In such cases the tracing that seemed more likely to be correct given the surrounding data was kept. The revision of the 2D migrated bedrock data reduced the maximum difference of crossing profiles from 108 m to 8 m.

There are various ways to construct bedrock DEM from RES-profile data. In recent studies on Icelandic glaciers (Magnússon *et al.*, 2012; 2016) the final bedrock DEMs have been produced by manually modifying elevation contours of a preliminary DEM obtained with kriging interpolation of the RES-data and then interpolating the final product using the modified contours as input for another kriging interpolation. This has been done to reduce artefacts of kriging interpolation from discrete RES-profiles as well as artefacts caused by the shortcoming of the 2D migrated RES-data described above. Applying this approach for a large and dense data set requires time-consuming manual work. The artefacts of the kriging methods are also substantially less prominent than in the case of more discrete RES-profiles, particularly after taking care of mismatch at crossing profiles as explained above. Alternatively, more sophisticated interpolation schemes, constrained by physical models and other input data such as glacier surface topography and velocity observations (e.g. Morlighem *et al.*, 2011; Fürst *et al.*, 2017), could be adopted. However, for a large portion of the study area these schemes would fail without substantial improvements, due to strong basal melting beneath ice cauldrons, which strongly affects the surface topography and motion.

Due to the complications of the above interpolation methods it was decided follow a relatively simple approach in the creation of the final bedrock DEM (with 20×20 m cell size). Kriging interpolation was applied in Surfer 13 (©Golden Software, LLC), with input data (coordinate list of easting, northing, bedrock elevation) consisting of the filtered and revised bedrock traces from the 2D migration, bedrock traces from the 3D migration, elevation of nunataks at their edges, elevation of the previous bedrock DEM (Figure 2b) at the edges of the study area and a few manually created elevation contours, drawn to obtain realistic landforms where RES-data is lacking (Figure 3). The bedrock DEM obtained with this interpolation was then mosaicked with the previously existing bedrock DEM outside our survey area and lidar DEM (Jóhannesson *et al.*, 2013, subsampled to 20× 20m cell size) of nunataks, resulting in the final product (Figure 6). The ice thickness map (Figure 7a) is calculated as the difference between a glacier surface DEM, obtained from Pléiades images in 28 September 2019, and the presented bedrock DEM.

Extraction of tephra layer data

The 2D migrated data from May 2016 and February 2017 along with 3D migrated data from 2017, (around K6, K7, K10, K11 and K16) and 2018 (K1 and K2) was used to map the ice thickness above the 1918 tephra layer. To compensate for the time difference between observations, data from 2017 and 2018 were shifted upwards by 3 and 6 m, respectively, to represent the year 2016. This is based on the crude assumption that the layer depth increases linearly with time; in 2016, almost a century after the eruption, the tephra layer was on average at ∼300 m depth. Given the variable depth of the layer and that the vertical motion is expected to decrease with depth (see discussion

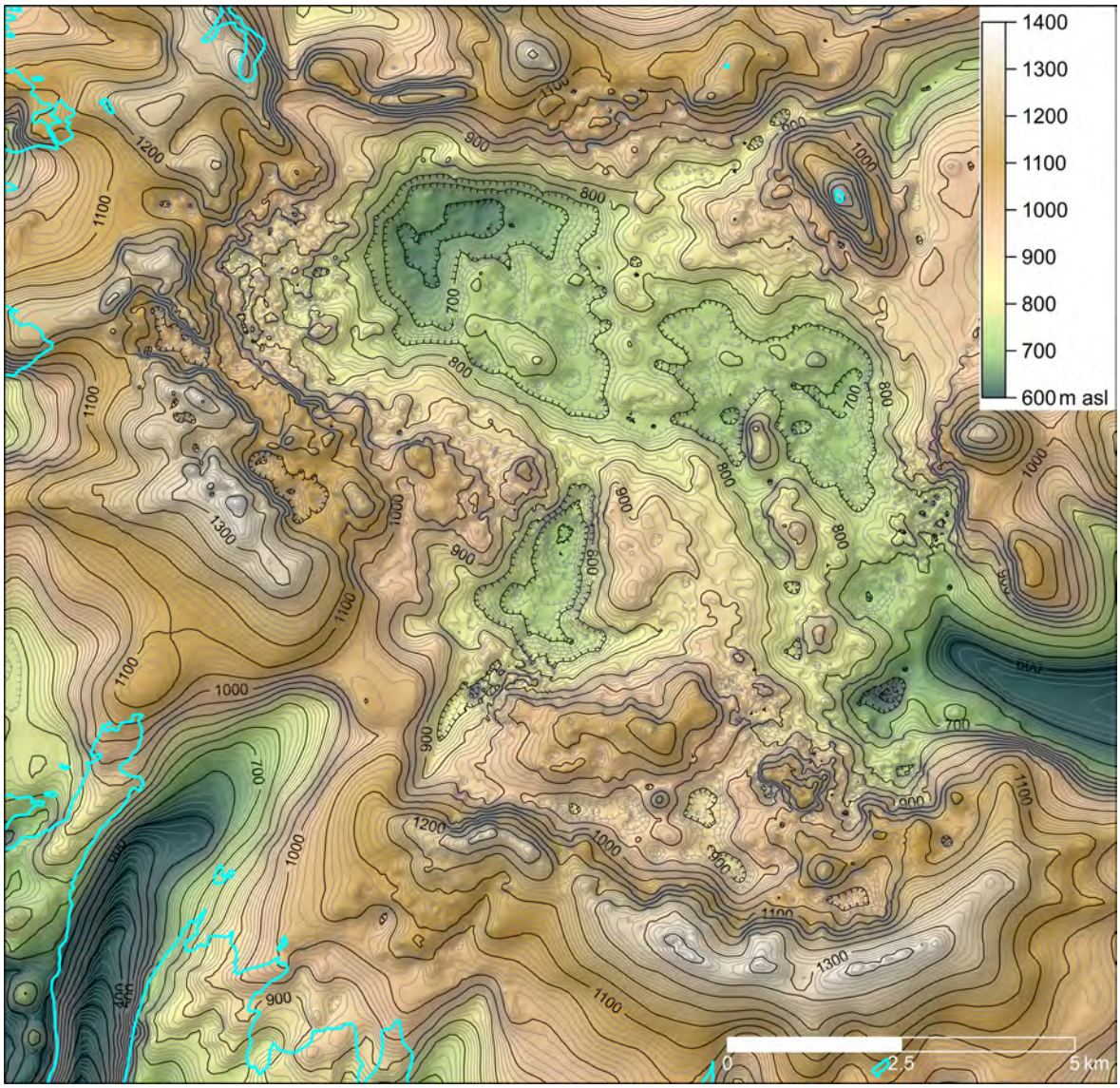

Figure 6. The new bedrock DEM of the study area shown as elevation contour map with 10 m contour interval. *– Nýtt botnhæðarkort (10 m hæðarlínubil) af svæðinu sem rannsóknin spannar.*

below on modelled ice motion and surveyed mass balance) we expect the upward projection of the tephra to the year 2016 generally has less than 50% error, corresponding to 1.5 and 3 m for the 2017 and 2018 data sets, respectively. When obtaining ice thickness above the older tephra layer found at greater depth in the northern part of the caldera, only 2D migrated data from 2016 were used.

The tracing algorithm used for bedrock was also applied to the tephra layer. In areas where the tephra

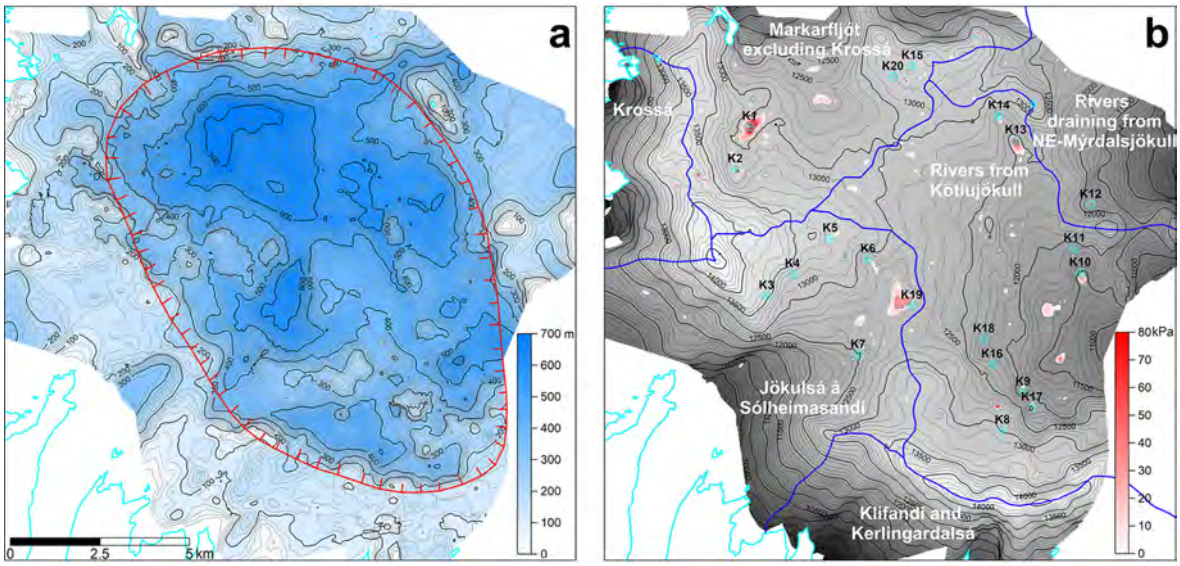

Figure 7. a) Ice thickness map of the study area calculated using the glacier surface in September 2019. b) Static water potential at the glacier bed, revealed as a greyscale image and a contour map (100 kPa contour interval equivalent to 10 m of hydrostatic head), calculated from the new bedrock DEM and glacier surface in September 2019. Blue lines show water divides between the labelled drainage basins, obtained from the potential map. The locations of cauldrons within different water drainage basins are shown. The red coloured image on top of the potential map indicates depth and size of closed depressions in the potential map forming local minima. *– Ísþykktar- (a) og vatnsmættiskort m.v. að jökull liggi á botni með fullu ísfargi (b) reiknað út frá jökulbotni (6. mynd) og jökulyfirborði í september 2019. Jafnmættislínur á mynd (b) eru með 100 kPa millibili (jafngildi 10 m hárrar vatnsssúlu). Bláar línur (b) sýna vatnaskil milli helstu vatnasviða samkvæmt vatnsmættiskorti og þar með hvaða sigkatlar falla innan hvers vatnasviðs. Rauðskalamyndin sem felld er ofan á mynd (b) sýnir stærð og dýpi lokaðra lægða í vatnsmættiskorti.*

layer was close to the glacier bed the migration of both the 2D and 3D data was repeated with all reflections likely to originate from the glacier bed masked out in the input data before the tephra layer reflections were traced. This was done due to limitations of the migration method, which in some cases produces weak artificial signals propagating upwards from the relatively strong bed reflections. This artefact was not a problem when tracing the bedrock reflections, but in some cases, it obscured the much weaker internal reflections near the bed. The masking was done by calculating for each survey point the distance from the transmitter to the nearest point in the final bedrock DEM and back to the receiver and the corresponding travel time, $t_{bed\_nearest}$ (with c_{gl}=1.68$\times$ 10^8 m s^{-1}) and then replacing all backscatter values with travel time >($t_{bed\_nearest}$ -1$\times$ 10^{-7} s) with 0. Assuming that the final bedrock DEM is accurate this should only leave internal backscatter originating >$\sim$10 m above the glacier bed. When tracing reflections from the deeper tephra layer and parts of the 1918 tephra layer, the tracing algorithm described above proved inefficient due to a low signal to noise ratio, causing the automatic tracing to fail repeatedly even though it could be traced from visual inspection. In those cases the tracing was carried out with manual digitization.

The traced tephra reflections in the 2D migrated data, were filtered and subsampled to values at 20 m intervals along the profile while the traced reflection from the 3D-migrated data was used unfiltered.

Again, results from 2D migrated data were not used if the area was covered with data from 3D migration. The result from both the 2D and 3D migrated RES-data was exported as a list of coordinates (easting, northing, tephra layer elevation). The tephra layer elevation tends to reflect the surface topography; hence variation in depth down to the tephra layer relative to the glacier surface is of more interest than the tephra layer elevation. A map of tephra layer elevation obtained by interpolating directly tephra layer elevation from discrete profiles would lack correlation with the surface elevation in areas where RES-data is missing. RES-profiles showing e.g. the tephra layer at approximately the same elevation on each side of an un-surveyed topographic surface high would result in a flat plane cutting through this high if the tephra layer elevation were interpolated. Consequently the depth to the tephra layer at the surface high would be overestimated. By interpolating the depth to tephra layer relative to the glacier surface, such artefacts are avoided. The tephra layer coordinate lists were therefore compared with surface elevation DEM obtained from Pléiades optical satellite images in 27 September 2016 to replace the third column of the lists (tephra layer elevation) with depth down to tephra layer relative to this surface DEM. This coordinate list was used as input into kriging interpolation to calculate an ice thickness map (grids with 20×20 m cell size) above the corresponding tephra layer (Figure 8a,b).

The detected tephra reflections are in most cases from gentle sloping layers directly beneath the survey profile, not due to cross-track reflections. Steep tephra slopes can occur, in vicinity of prominent cauldrons, where strong subglacial melting bends the glacier isochrones towards the glacier bed. The 1918 tephra layer is extractable from the 3D migrated data near most of the ice cauldrons. The most prominent exception is in the vicinity of K13 and K14, where only 2D migrated data was available and used uncorrected, since the difference in tephra layer depth at the few crossing profiles was within ∼10 m. However, the width of the depression in the tephra layer near these cauldrons may be underestimated by several tens of metres. This shortcoming of the 2D migrated RES-profile also explains a ∼10 m difference between tephra layer depths for crossing profiles at the centre of K19. The shallower trace was considered as cross-track reflection and omitted, but the deeper one a reflection from tephra layer directly below the radar and therefore included in the record used as input into the tephra layer interpolation.

RESULTS AND RELATED DISCUSSIONS

Topographic features

Primary results lie in a revised DEM of the glacier bed (Figure 6) and a map of ice thickness within the caldera (Figure 7a), confirming the main features of the older DEM (Figure 2b) and the thickest ice in the northern part of the caldera, to be up to 740±40 m, in accordance with previous studies (Björnsson *et al.*, 2000). Uncertainty of 5% is assumed, mostly due to uncertain c_{gl} (Lapazaran *et al.*, 2016), which has not been measured specifically for the study area. The amount of ice within the caldera rim (as defined by Björnsson *et al.*, 2000) was 45±2 km^3 in September 2019. The complex topography within the caldera described in Björnsson *et al.* (2000) is further high-

8. mynd. – *a,b) Kort af þykkt íss í september 2016 ofan 1918 gjóskulagsins (a) og eldra gjóskulags í norðurhluta öskjunnar (b). Kortin eru brúuð út frá gjóskulagsendurköstum sem greinast í íssjármælingunum en staðsetningar þeirra eru sýndar sem gráar línur (tvívíð staðsetningarleiðrétting) og skellur (þrívíð staðsetningarleiðrétting). c) Dæmi um tvívítt staðsetningarleiðrétt íssjársnið, frá A til B á mynd (a), þar sem greina má endurkast frá báðum gjóskulögunum auk endurkasts frá botni. d) Snið á ísaskilum Entujökuls og Kötlujökuls (frá C til D á b og á innskotsmynd) sem sýnir brúaða botnhæð og gjóskulög í september 2016. Til samanburðar er sýnd lega jafnaldurslaga reiknuð miðað við æstætt hreyfisvið á þeim stöðum sem íssjársnið þvera ísaskilin (innskotsmynd sýnir hvar gjóskulags og botnendurköst greinast í nágrenni þeirra). Yngstu reiknuðu lögin svara til gosa sem gætu hafa skilið eftir sig gjóskulög sem enn greinast með íssjá í jökulísnum.*

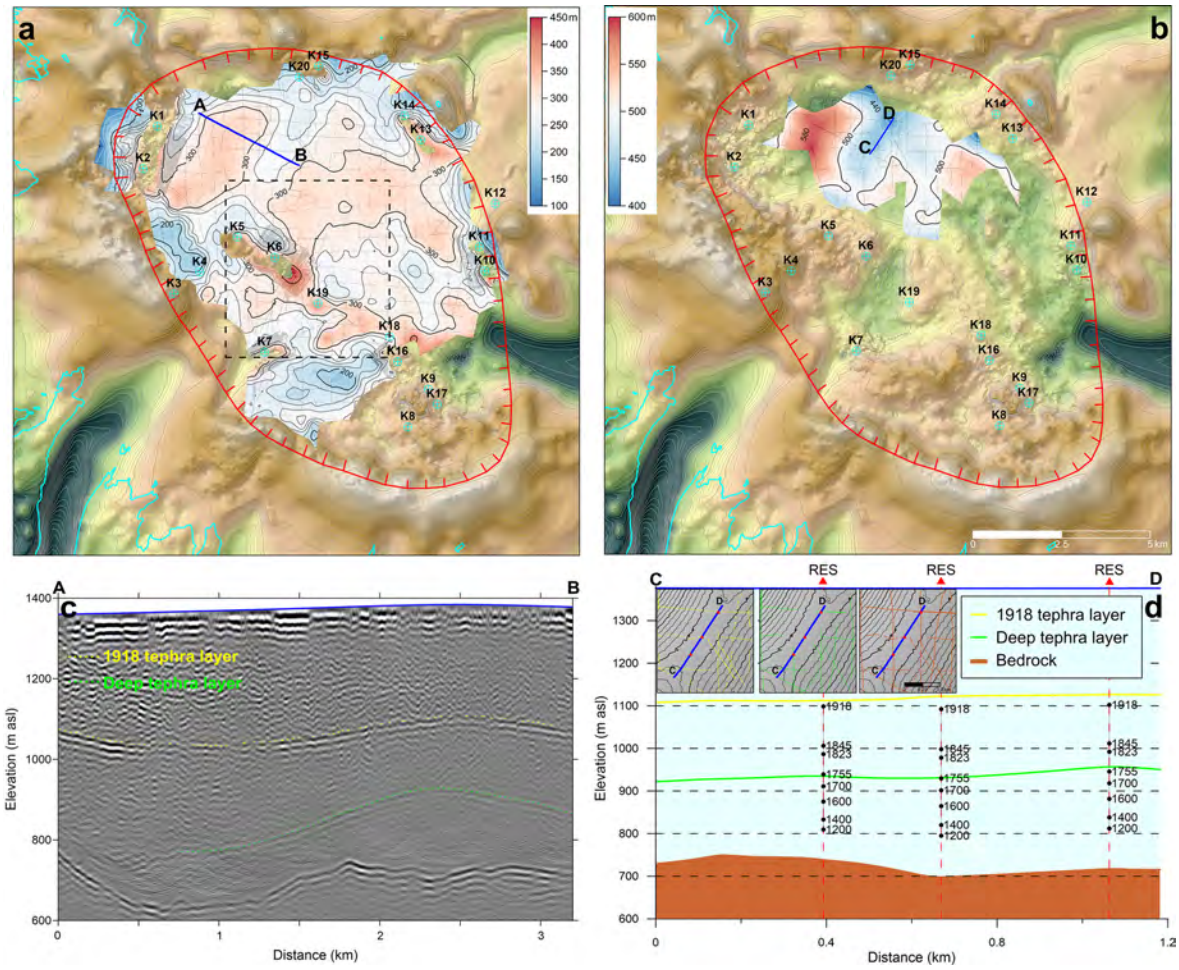

Figure 8. a,b) Interpolated maps showing ice thickness above the 1918 (a) and a deeper tephra layer (b) in September 2016. Grey lines and clusters indicate locations of traced tephra layer reflection. The dash-lined box in a indicates the area zoomed in on Figure 11. c) An example of 2D migrated RES-profile, location from A to B (a) showing both tephra layers and bedrock. The image is a mosaic of a 2D migrated profile, applying masking of bedrock reflections prior to migration (see Data and Methods for further details) for the englacial reflections, and the normal 2D migrated profile without masking of bedrock reflections; the grey scale image for the englacial reflections corresponds to weaker backscatter than for the bedrock reflections. d) Cross-section at the ice divides between Entujökull and Kötlujökull, from location C to location D on (b), and inserted images) showing the glacier surface in September 2016, the interpolated bedrock and the interpolated tephra layers in September 2016. For comparison, the elevation of various isochrones, obtained from a static velocity field (Jarosch *et al.*, 2020; see main text for further details), are shown for September 2016 at three locations where RES-profiles cross the ice divides. The inserted images indicate the locations of traced bedrock and tephra layer reflections.

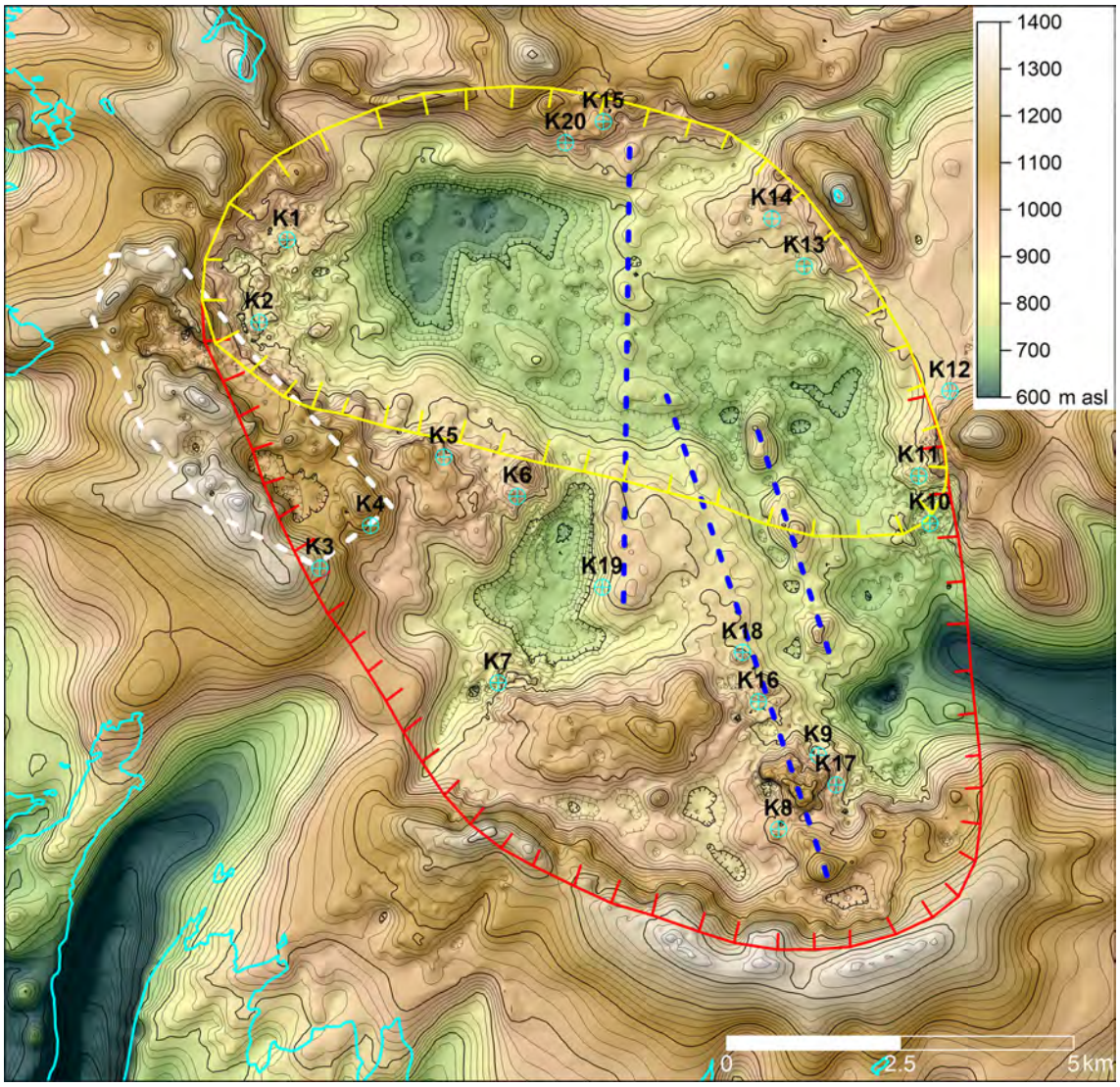

Figure 9. Highlighting of some topographic features observed in the new bedrock DEM (shown as contour map with 20 m contour interval) such as rows of peaks with north-north-westerly and northerly directions (dashed blue lines), suggested rim of a sub-caldera (the yellow hachured polygon) within the main caldera (the red hachured polygon) and area of sharp depressions near Goðabunga, partly surrounded with 100–200 m high cliff faces (dashed white line). – *Helstu drættir í nýju botnhæðarkorti (20 m hæðarlínubil), þar á meðal raðir hæða og fella sem liggja frá suðri til norðurs eða suðsuðaustri til norðnorðvesturs (bláar brotalínur) og brún mögulegrar öskjumyndunar (gul hökuð lína) innan megin öskjunnar (rauð hökuð lína). Einnig er afmarkað svæði við Goðabunga (hvít brotalína) þar sem er að finna djúpar lægðir sem virðast umluktar 100–200 m háum hamraveggjum.*

lighted by the new bedrock DEM. Topographic features such as rows of peaks with north-north-westerly and northerly directions were visible in the old DEM (Figure 2b). These features, which may be formed during fissure eruptions within the caldera are revealed in more detail in the new DEM (Figure 9). Five ice cauldrons are clustered along one of these lines. The caldera rim has approximately elliptical form with its major axis aligned from south-east to north-west splitting the caldera into the north-eastern and the south-western halves. The more rugged and elevated terrain in the south-western half, compared with the substantially deeper north-eastern half, was attributed to higher eruption rate, since the volcano became ice covered (Björnsson *et al.*, 2000). These topographic characteristics, now even more clearly defined by the new bedrock DEM, also raise the question whether the Katla caldera is a single caldera formation or if smaller caldera formations exist within the main caldera. The most conspicuous candidate is a large depression defined by the main north caldera rim and the steep mountainside with up to 200 m topographic relief that is aligned east-south-east and crosses the centre of the main caldera. The suggested sub-caldera, outlined in Figure 9, has an area of $\sim$45 km^2, corresponding to almost half the main caldera area. If we assume this sub-caldera was formed during a caldera collapse event (or repeated events) overprinting the large main caldera the volume of the sub-caldera formation can be estimated by studying how much the mean elevation of the sub-caldera floor ($\sim$820 m asl) differ from the mean elevation of the main caldera floor when the suggested sub-caldera is excluded ($\sim$930 m asl). This correspond to a volume of 5 km^3. The suggested sub-caldera formation is situated above the Katla magma chamber as inferred from seismic undershooting (Guðmundsson *et al.*, 1994). Another possible sub-caldera formation is $\sim$5 km^2 depression between K6, K7 and K19 slightly south of the caldera centre (Figure 9). It is $\sim$250 m deep relative to its surroundings and is close to a suggested location of the 1755 Katla eruption site (Björnsson *et al.*, 2000). Thirteen out of the 20 established ice cauldron locations are close to the rims of these two suggested caldera formations.

The new bedrock DEM also reveals some previously unknown topographic features. The most prominent of those are sharp depressions near Goðabunga at the west-rim of the caldera (area outlined with dashed white line in Figure 9). The depressions are up to 250 m deep and partly surrounded with 100–200 m high cliff faces. These structures, which do not align with likely glacier motion along the glacier surface slope, do not resemble features carved by glacier erosion. It is more likely that they are either a complex set of ridges formed by eruptions beneath the glacier or collapse structures. To better understand the nature of these features a denser RES-survey of this area is required for further improving the bedrock DEM of this area, ideally with 3D migration since these steep wall structures are hard to map accurately from 2D migrated RES-data. An example of topographic mapping of similar structures is shown in Figure 10 where 3D migration reveals a $\sim$200 m high cliff face of a mountain east of K9. This cliff is not formed by glacier erosion since it opposes the ice flow from a higher part of the glacier south-west of the mountain. This mountain, which is the most prominent feature in a previously mentioned row of peaks (Figure 9) is likely formed by an eruption and further carved by ice-volcano interactions. This area was initially surveyed with dense profiling allowing 3D migration as it was assumed to be likely location of the 1918 eruption. However, recent work (Gudmundsson *et al.*, 2021; Larsen and Högnadóttir, 2021) locates the main eruption site of 1918 to be $\sim$1 km east of this area, which was densely surveyed with RES in May 2021 (see Addendum).

DEMs from 3D versus 2D migrated RES-data

The DEMs obtained from 3D migrated RES-data highlights the limitation of 2D migrated data in areas of steep and rugged bedrock topography. Such a comparison is given in Figure 5 showing the difference between results from 2D migrated RES-survey carried out in the spring 2016 around K6 and from 3D migrated survey carried out in spring and autumn 2017. The 2D migrated bed traces are on average $\sim$10 m higher, with $\sim$20 m standard deviation of the elevation difference, when compared with the 3D migrated DEM (Figure 5c). Similarly, when a bedrock DEM

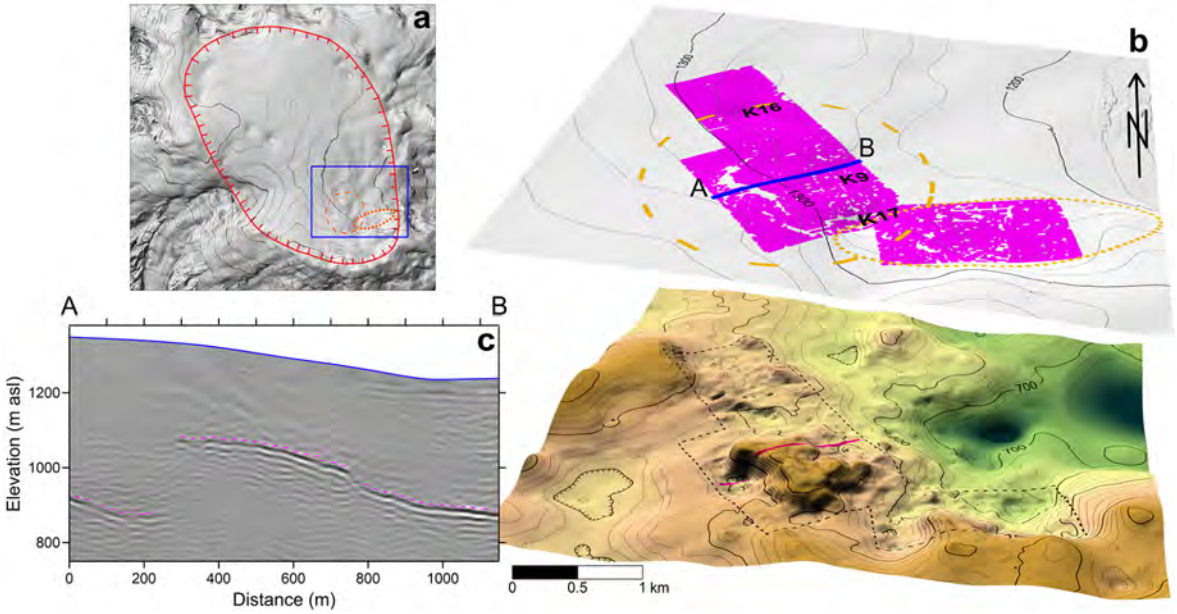

Figure 10. A close up of the area around K16, K9 and K17 (shown with a blue box in a) showing 3D representation of the glacier surface (in September 2016) and bedrock (b). The magenta coloured cluster on the surface 3D image, indicates location of traced bedrock reflections from the 3D migrated RES-data. The corresponding area is outlined with a dashed black line on the 3D bedrock image. The RES-survey of K9 and K17 in 2019 focused on the area considered in Björnsson *et al.*, (2000) as the location of the 1918 eruption, orange dash lined circle in (a) and (b). More recent study (Gudmundsson *et al.*, 2021) however locates the eruption further east (orange dot lined ellipse in a and b). Large part of that area was surveyed with dense RES-profiling in May 2021 (more info on Figure 12). c) 3D migrated RES-profile crossing a mountain west of K9 (profile location from A to B shown in b) revealing 250 m high cliffs on the west side of the mountain (dashed magenta line indicates traced bed reflections). The RES-profile (c) and the 3D images (b) are without vertical exaggeration. – *Nærmynd af svæðinu nærri kötlum 16, 9 og 17 (afmarkað með bláu boxi á mynd (a)) sem þrívíddarmynd af jökulyfirborði og botni (b). Purpurarauðu skellurnar á yfirborðinu sýna staðsetningar greindra botnendurkasta í íssjársniðum unnar með þrívíðri staðsetningarleiðréttingu á endurkastsflötum. Tilsvarandi svæði er sýnt með svartri brotalínu á botni. Íssjármæling umhverfis katlana vorið 2019 beindist að svæði sem talið var gosstöðvarnar 1918 (Helgi Björnsson o.fl., 2000) innan hringlaga appelsínugulrar brotalínu á myndum (a) og (b). Samkvæmt nýrri rannsókn (Magnús T. Guðmundsson o.fl., 2021) voru gosstöðvarnar líklega að mestu bundnar við svæði nokkru austar, innan sporbaugslaga appelsínugulrar punktalínu á myndum (a) og (b) en stór hluti þess svæðis var mældur í maí 2021 (sjá 12. mynd). c) Íssjársnið með þrívíðri staðsetningarleiðréttingu, yfir fjall vestur af katli 9 (frá A til B á b), sýnir um 250 m háa hamra í vesturhlíðum fjallsins (purpurarauð brotalína afmarkar greind botnendurköst). Bæði þrívíddarmyndin (b) og sniðið (c) eru án hæðarýkingar.*

created by kriging interpolation from 2D migrated bed traces is compared to the 3D migrated DEM, the difference is also on average ∼10 m higher with ∼20 m standard deviation (Figure 5d). Most of this difference can be related to the previously mentioned limitation of the 2D migrated data (see Data and Methods), caused by cross-track bed reflections interpreted as being located directly beneath the radar, while the actual bed at the same location is often tens of metres lower (up to 100 m for the data shown in Figure 5). The main exception, where the limitation of the 2D migrated data does not explain this, is at the location

of the magenta coloured points in Figure 5c, denoting bed interpreted from the 2D migrated profile, more than 80 m below the bed derived from the 3D migrated data; generally the 2D migrated traces are above the 3D migrated DEM due to cross-track reflections. This was due to wrong interpretation of bed reflection in the 2D migrated data. The first strong reflection near the bed in the 2D migrated profiles was considered to be a reflection from the top of a water chamber directly beneath the centre of K6. A reflection at greater depth, considered to be from the bed directly beneath, was in this case likely a strong cross-track reflection from a mound 300 m NNE of this location. The actual bed directly beneath the radar was probably screened by the water body in spring 2016.

This comparison demonstrates that using 2D migrated RES-data, without any adjustments to compensate for the effects of cross track reflections, will result in an upward bias of the resulting bed DEM for steep and rugged bed terrain. The 10 m offset of 2D migrated RES-data for this area is too high to be explained by other systematic errors. Accurately repeated surveys, both the 3D migrated surveys presented here and repeated 2D migrated profiles surveyed on Mýrdalsjökull and Vatnajökull (Magnússon *et al.*, 2017; 2021) suggest that temporal variations due to such errors are generally less than 3 m from one survey to another. A similar experiment comparing 2D and 3D migrated RES-data obtained above steep bedrock beneath Gulkana Glacier, Alaska, also indicated a similar underestimate in bed elevation from the 2D migrated data (Moran *et al.*, 2000). The comparison presented here also shows that if the effects of cross track reflections are not considered, measuring a denser set of profiles than done in 2016 for K6 and vicinity ($\sim$200 m between profiles) would not have much increased the accuracy of the interpolated DEM. The DEM accuracy had already reached the accuracy of the input data used in the interpolation. This suggests that the interpolation errors were insignificant in comparison with the errors caused by the limitations of the 2D migration. The benefit of profiles denser than 200 m apart for similar radar set-ups in areas of comparable bed slopes and ice thickness (300–600 m) are likely small if the effects of cross track reflections are not considered. For more gentle slopes, denser profiles can improve the resulting bedrock DEM.

In our study, the difference at the crossing points of the 2D migrated profiles has been used to adjust the location of traced bed reflections for the profiles that are likely to be substantially affected by cross-track reflections, before carrying out the bedrock interpolation (see Data and Methods and Figure 3). We expect our simple approach to substantially reduce the errors caused by cross-track reflections, but we still expect significant errors of this kind to remain in our bedrock DEM in steep areas.

Water potential and drainage basins

Using the new bedrock DEM and the surface DEM from 2019, with 20$\times$ 20m cell size, the water divides between drainage basins (Figure 7b) were updated from previous work (Björnsson *et al.*, 2000, and more recent unpublished work of IES-glaciology group) within the study area. This was done by assuming that the water flow along the gradient of the static water potential, φ, at the glacier bed with water pressure corresponding to the full ice overburden pressure (e.g. Björnsson, 1975):

$$\varphi=\rho_w g z_b + \rho_i g H \qquad \text{Eq. 1}$$

where ρ_w=1000 kg m^{-3} and ρ_i=900 kg m^{-3} is the density of water and ice, g=9.82 m s^{-2} the acceleration due to gravity and z_b the bedrock elevation. $H = z_s - z_b$ is the ice thickness where z_s is the surface elevation. The procedure of drawing water divides, as explained in Magnússon *et al.* (2012), includes filtering of the surface DEM with a circular filter prior to calculating the water potential. The filter weight decreases linearly to zero at distances corresponding to half ice-thickness, hence it is assumed that due to the strength of the ice, the weight of an ice column affects the ice overburden pressure over a distance equal to the ice thickness. The filter smooths out noise and small scale errors in the DEM as well as actual small scale features such as crevasses. The revision of the water divides (Figure 7b) shifts them in some cases a few hundred metres from the ones presented by Björnsson *et al.* (2000). Substantial part of this change is not related to the improved bedrock DEM but to difference between surface DEMs; the change

is much less when compared with unpublished water divides made by IES-glaciology group, using the old bedrock DEM (Figure 2b) and the lidar surface DEM from 2010 (Jóhannesson *et al.*, 2013). The DEM from 2010 both resembles more the 2019 glacier surface and is much more accurate than the surface DEM used in Björnsson *et al.* (2000), which was based on measurements in 1991.

The known geothermally-sustained cauldrons are all within the drainage basins of the rivers Markarfljót, Jökulsá á Sólheimasandi or the rivers draining from Kötlujökull, except K12, which drains to river Leirá draining from northeast Mýrdalsjökull. All cauldron locations fall within the same drainage basins for both the previous (Björnsson *et al.*, 2000 and the unpublished one using the 2010 lidar survey) and the new delineation, with the exception of K19. This cauldron now falls within the drainage basin of the river Jökulsá á Sólheimasandi but had previously fallen within the Kötlujökull drainage basin in previous estimates of the water divides. It should be noted, however, that the water divides at this location are very sensitive to errors in input data and the assumptions made when estimating the water potential. Hence it is quite uncertain to which drainage basin K19 belongs. The same applies to K5 and K6 as the estimated drainage route from these cauldrons passes below K19. However, it is fairly certain to which drainage basins all the other cauldrons belong.

The derived water potential has many local minima, which can be viewed as puddles in the potential, facilitating water accumulation at the bed. These puddles are typically found beneath the geothermally sustained cauldrons (Figure 7b). It should however be noted that potential puddles are also found outside known cauldron locations. Beneath some of the cauldrons, known to release water in jökulhlaups, either no or only small and shallow potential puddles are derived. This even applies for cauldrons where the bed has been obtained from 3D migrated RES-data, including cauldrons K16, K9 and K11 (the applied surface filtering mentioned above only slightly reduces the size and the depth of the potential puddles). K9 and K11 are located above steep beds, which almost evens out the effects of adverse surface slope out of the cauldron despite surface slope, having 10-fold stronger influence on the potential gradient ($\nabla\varphi$) than the bed slope. In the case of K16 it did not form a closed surface depression in September 2019, causing the absence of a potential puddle. Comparison between DGNSS data obtained during the RES-survey in May 2019 and the September surface DEM does however show that water was released from beneath K16 during the summer, causing up to 10 m lowering in the cauldron centre, despite the lack of a potential puddle. This highlights the limitation of using Eq. 1 to locate potential sources of jökulhlaups. These limitations should be studied further by comparing cauldron activity and how the estimated water potential varies with time, both seasonally and over longer time scales, using various available surface DEMs obtained since 2010, as well as the new bedrock DEM.

Tephra layers

The maps of ice thickness in 2016 above two tephra layers (Figure 8) observed at depth within the caldera should also be considered as one of the main results of this study. The older tephra layer is only observed in the northern part of the caldera, within the thickest part of the glacier and was found at 390–600 m depth in 2016. The younger layer at shallower depth is tephra that fell on the glacier surface during the 1918 eruption (Brandt *et al.*, 2006) and is still stored in the ice within most of the caldera. The largest exception is the southeast part of the caldera (Figure 8a). The gap in the presented map is partly related to lack of RES-data (the area south of K10 above the trough towards Kötlujökull), but for the main part of the area surrounding K8, K9, K16 and K17 the tephra layer is not observed in the RES-data. At the boundary of the area where the 1918 tephra layer is observed, north of these cauldrons, the layer dips towards the glacier bed and can be traced until it is 30–100 m above the bed. It is therefore likely that for a large proportion of the area around these cauldrons, where the tephra layer is not seen in the RES-data, the 1918 tephra layer has already reached the glacier bed, due to geothermal activity and relatively shallow ice. It likely also plays a role that the 1918 eruption took place in this area (Gudmundsson *et al.*, 2021) resulting in even thinner ice right after the eruption. Geothermal activity has

also brought the tephra layer down to the glacier bed, beneath many cauldrons, revealed as data gaps in Figure 8a. It is not always clear what causes the absence of the 1918 tephra layer in other areas but the glacier in these areas is often relatively thin (e.g. areas near Goðabunga at the south-west rim of the caldera and survey areas outside the caldera).

In 2016, the 1918 tephra layer lay mostly at 200–350 m depth, in few areas at less than 200 m depth, but in the westernmost part of the survey area, the tephra was at ∼100 m depth (Figure 8a). This shallow depth of the layer, almost 100 years after the eruption, is noteworthy given that the annual balance, measured at the peak of Goðabunga ∼3 km further south, is typically between 3 and 4 m ice equivalent (Ágústsson *et al.*, 2013 and more recent unpublished data from JÖRFÍ field surveys). A recent study applying snow radar to map winter accumulation did however indicate ∼40% less winter snow in the area of minimum tephra layer depth in May 2016 than at the peak of Goðabunga (Hannesdóttir, 2021). This is probably a persistent accumulation pattern produced by redistribution due to snow drift (e.g. Dadic *et al.*, 2010) reducing winter accumulation at a ridge between the caldera plateau and the west side of Mýrdalsjökull, explaining the shallow depth of the tephra at this location (Hannesdóttir, 2021).

The topography of the 1918 tephra layer within the ice is clearly shaped by subglacial geothermal activity. A good example is the area at the caldera centre, where the subglacial geothermal activity, beneath K5, K6, K7 and K19, clearly leave their imprints in the 1918 tephra layer (Figure 11). We also observe a strong depression in the tephra layer south of K19 (also seen as a dip in the traced tephra layer on Figure 2e). This (marked A in Figure 11) is not a location of previously known cauldron, although there is a clear curve in the surface contour lines matching the location of the depression in tephra layer. Subglacial melting due to geothermal activity seems required to explain these features. Another less obvious feature is a ∼25 m deep depression in the tephra layer north of K6 (marked B in Figure 11). This depression is also observed in the deeper tephra layer at this location (Figure 8b). At first glance, this shallow depression seems likely to be formed by ice dynamics. However, comparison of the glacier surfaces from 2016 (Pléiades) and 2010 (Jóhannesson *et al.*, 2013) shows that minor curves in the surface elevation contours at this location in 2016 were substantially stronger in 2010; the surface undulation at this location has been smoothed from 2010 to 2016. This shallow depression in the tephra layer is therefore likely an imprint of weak and probably sporadic geothermal activity at the glacier bed, which may have been dormant in 2010–2016.

The beautiful depression in the 1918 tephra layer formed by the subglacial geothermal activity beneath K6 includes the 1918 tephra observed at greatest depth (∼460 m) southeast of the cauldron. This depression becomes shallower, reaching a saddle point ∼1.4 km southeast of K6 centre (marked C in Figure 11). To understand the formation of the saddle point, results from recent modelling work, carried out to estimate the power of the geothermal areas beneath the ice cauldrons of Mýrdalsjökull in 2016–2019 (Jarosch *et al.*, 2020) were inspected. In the modelling, 3D-velocity fields for the slow, gravity driven flow of ice were computed with the stationary incompressible Stokes equations (see e.g. Jarosch, 2008 for details). The modelling used the bedrock DEM, presented here (without improvements from the 2021 RES-survey around the 1918 eruption site), and annual surface DEMs in 2016–2018 (from Pléiades autumn images) as inputs. The rate factor A in Glen's flow law (Glen, 1955) was tuned by fitting the model output velocity with results from GNSS stations at various location including stations at K6 centre in 2018, resulting in A=2.6$\times$ 10^{24} Pa^{-3} s^{-1}. A textbook value of n=3 (e.g. Cuffey and Paterson, 2010) was assumed for the nonlinearity exponent in Glen's flow law. From the velocity field in September 2016, modelled using surface DEM from the same month, we obtain horizontal surface velocity between 6 and 9 m a^{-1} along an approximate flow line between K6 centre and the saddle point C. Assuming that this velocity is representative for the ice motion at this location since 1918, this indicates that tephra now at C fell on the glacier surface in 1918 only 600–900 m closer to K6 or at least 500 m southeast from the cauldron centre. This tephra did therefore not pass the area where most of the down-

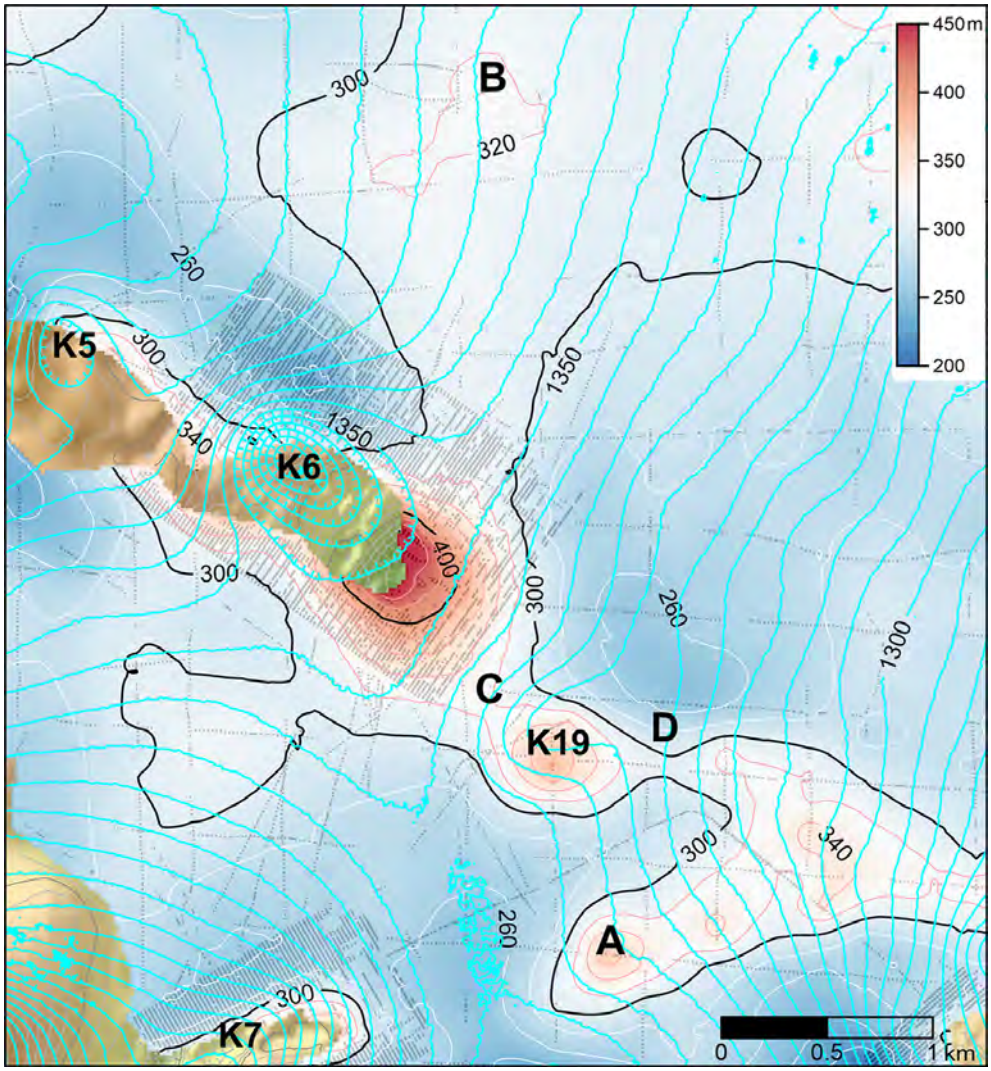

Figure 11. Zoom in on the map of ice thickness above the 1918 tephra layer in 2016 (area shown in Figure 8a), overlain with cyan contour map showing the glacier surface (5 m contour interval) in September 2016. A, B, C and D indicate locations of special interest discussed in the main text. – *Nærmynd af þykktarkorti íss ofan 1918 gjóskulagsins í september 2016 (útmörk nærmyndar eru sýnd á 8. mynd a). Ofan á þykktarkortið hafa verið felldar blágrænar yfirborðshæðarlínur sem sýna yfirborð jökulsins (5 m hæðarlínabil) í september 2016. Staðir merktir A og B eru svæði þar sem líklega er áður óþekkt jarðhitavirkni sem skapar lægðir í gjóskulaginu frá 1918. Staðir C og D eru söðulpunktar í ísflæðilínum frá kötlum 6 og 19; gjóskan liggur hærra undir þessum punktum en annars á sömu ísflæðilínu bæði nær og fjær jökulsporði. Líklegar skýringar þessara söðulpunkta eru mismunandi: Hægt ísflæði skýrir líklega C. Gjóskan sem nú er undir C féll líklega á jökullinn milli ketils 6 og C utan megin áhrifasvæðis jarðhitans sem myndar ketilinn. Þessi skýring á ekki við í tilfelli D og því er líklegt að þar sé um að ræða breytilega virkni í jarðhita. Virkin undir katli 19 hefur líklega verið mun minni en nú á löngum tímabilum á 20. öld.*

ward dragging, caused by subglacial melting beneath K6, occurs. Down-glacier from point C, the time integrated downward drag, due to the geothermal area beneath K19, increases.

The saddle point down-glacier from K19 (marked D) is however hard to explain in same way as for the one at C. The higher velocity and shorter distances indicate that tephra now at D fell up-glacier from K19 and therefore passed the current geothermal area beneath K19 without much downward dragging due to subglacial melting. Saddle point D is therefore likely a sign of sporadic geothermal activity beneath K19.

Dating of the deeper tephra layer

The horizontal surface velocity at the part of the ice divide between Kötlujökull and Entujökull, shown in Figure 8b and 8d (indicated with blue line from point C to point D) , is 0–3 m a^{-1} in the model simulation for the glacier surface in September 2016, explained above (Jarosch *et al.*, 2020). The motion is along the ice divides towards a saddle point in the flow where ice motion is only vertical (downwards). This is therefore an ideal location to estimate the age of the deeper tephra layer by comparison of the downward vertical motion from the model simulation with the depth of the tephra layer. Doing so requires the assumption that glacier geometry as well as the ice flow remains fixed. For this to hold true the annual mass balance (in metres of ice equivalent) should equal the annual downward motion at the divides. The model results in an average downward motion of 4.3 m a^{-1}, for the line between C and D on Figure 8b, while the annual mass balance measured ∼900 m northeast of profile end D, was on average 3.9 m of ice equivalent, for the 11 successful years of measurement in the period 2001–2020 (Ágústsson *et al.*, 2013 and more recent unpublished data from JÖRFÍ field surveys). Assuming that both the obtained mass balance required to maintain equilibrium is correct and that the average of obtained mass balance measurements is representative for the period and this part of the ice divide (Figure 8b), would mean that the annual mass balance in ice equivalent has been 0.4 m a^{-1} too low during this 20 year period to maintain the elevation of the ice cap at this location.

By calculating the cumulative downward ice motion of the stationary velocity field with time we can estimate the age of the ice with depth and compare results with the depth of the two tephra layers. Figure 8d displays the estimated depth for tephra layers from the 1918, 1823 and 1755 eruptions of Katla as well as the 1845 eruption of Hekla at the location where RES-profiles were surveyed across the ice divides. This estimate results in the 1918 tephra layer at 15–30 m greater depth than the observed depth of the 1918 tephra. This may be partly explained by the glacier being thicker in 1918 than at present causing the starting elevation of the tephra layer to be higher than the one assumed in this model. In 1960 the glacier surface in this area was ∼15 m higher than in 2016 (Belart *et al.*, 2020), hence a 20–30 m higher glacier surface in 1918 than in 2016 seems likely. It should be noted, however, that thicker ice would likely also result in faster downward motion, which would partly compensate for the effect of a higher starting elevation.

When the possible candidates for the deeper tephra layer are considered, the estimated depth of a layer from 1755 fits almost perfectly the observed depth of the deep tephra layer. The eruption in 1755 was probably the largest eruption in Katla since the Eldgjá eruption in the 10th century (Larsen *et al.*, 2013) maybe apart from the eruption in 1918 (Larsen *et al.*, 2021; Gudmundsson *et al.*, 2021). The eruption in 1755 is therefore likely to have deposited a thick tephra layer on the glacier surface. Therefore, it is unlikely that tephra from smaller eruptions prior to 1755 and therefore at greater depth (e.g. the 1721 Katla eruption) would be detected if the 1755 tephra were not. Tephra falls on to the glacier surface from eruptions occurring between 1755 and 1918 probably all formed relatively thin layers not detectable with our radar; these were all either relatively small Katla eruptions (Larsen *et al.*, 2013) or originating from other volcanoes than Katla. The almost exact match of the modelled depth for 1755, while the match is poorer for 1918, could be due to net growth of the glacier in the period 1755 to 1918 (e.g. Björnsson, 2017). The starting elevation of the tephra falling in 1755 may have been closer to the 2016 glacier surface than the one in 1918. On average the mass balance in the pe-

riod 1755–2016 was close to the one required to maintain the present elevation at these ice divide, while it was above this value in the period 1755–1918, resulting in net elevation gain and below it in 1918–2016 resulting in net lowering.

The good agreement between the depth of the 1755 layer from the static modelled velocity field and the depth of the deep tephra layer, which independent of the model result is quite likely to be formed by the 1755 eruption of Katla, raises the question: How old is the ice below the tephra layer, which we mark as 1755? With the same method, we would approximate the elevation of ice made from snow falling on the glacier in 1200 AD to be somewhat less than 100 m from the glacier bed. However, our model does not include basal melting, so older ice will not be considered. Given the good agreement between the modelled and observed depth of tephra layers, as well as recent work estimating basal melting of Icelandic glacier (Jóhannesson *et al.*, 2020) we consider it unlikely that the annual basal melt rate beneath these ice divides (Figure 8b and 8d) is higher than 0.1 m a^{-1} (90 m of ice since 1200 AD); at present no clear cauldrons formed by subglacial geothermal activity are at this location. Our age estimate should, however, be considered with caution due to the assumption of fixed glacier surface; the glacier is expected to have been substantially thinner for a good part of the period since 1200 AD (e.g. Björnsson, 2017). With that in mind we still consider it likely that the age of the ice near the bed at the ice divides is 600–800 years or even higher. Applying time-dependent models for Mýrdalsjökull with varying geometry and mass balance should provide further constraints on this. Models aimed to simulate the development of Mýrdalsjökull and its mass balance in the past centuries should ideally use the constraint given by the depth, at the ice divides, down to the 1918 tephra layer as well what we identify as the 1755 tephra layer.

CONCLUSIONS

The comprehensive RES-surveys presented here have resulted in a revised bedrock DEM of the Katla caldera, which is unprecedented in terms of details for an ice covered volcano, particularly in areas where dense survey profiles allowed for 3D migration of the RES-data. It has also resulted in unique maps, showing the topography of two tephra layers, buried in ice, that have been shaped by subglacial geothermal activity and high surface mass balance rates, since 1918 for the younger tephra layer and since 1755 for the older layer, according to our dating. In addition to presenting these new results and describing in detail how they were obtained, we have listed and discussed various interesting features revealed in the bedrock and tephra layer topography. Further studies are required in many cases to understand some of these features, including various topographic structures beneath the glacier, or whether some observed shapes in the tephra layers are caused by geothermal activity, ice dynamics or spatially variable surface mass balance. The presented data sets will serve as vital input in various new studies, aiming to better understand subglacial geothermal activity, ice cauldrons, ice dynamics, subglacial hydrology and jökulhlaups, as well as the link between all these processes. Such studies have already started (e.g. Jarosch *et al.*, 2020). Furthermore, the detailed bedrock DEM and the topographic mapping of the dated isochrones within the glacier may serve as key data for studying the development and mass balance of Mýrdalsjökull in the past centuries.

Addendum: The bedrock topography at the estimated location of the 1918 eruption

Results from a recent study (Gudmundsson *et al.*, 2021) have led to relocation of the 1918 eruption to a site outside the span of the RES-data acquired in 2012–2019. It was therefore decided to carry out more RES-surveying in this part of the Katla caldera in May 2021. This included both a $\sim$1 km^2 area, surveyed with dense RES-profiles allowing for 3D migration, as well as 15 km of 2D migrated profiles (Figure 12a). The survey was carried out after the acceptance of this paper for publication in Jökull but despite this the new RES-data has been incorporated into the text, figures and tables of this paper, without changing any of the main findings presented above.

The bedrock map of the area specifically measured in 2021 (Figure 12b) is also shown as 3D representation in Figure 10b and on the cover image of

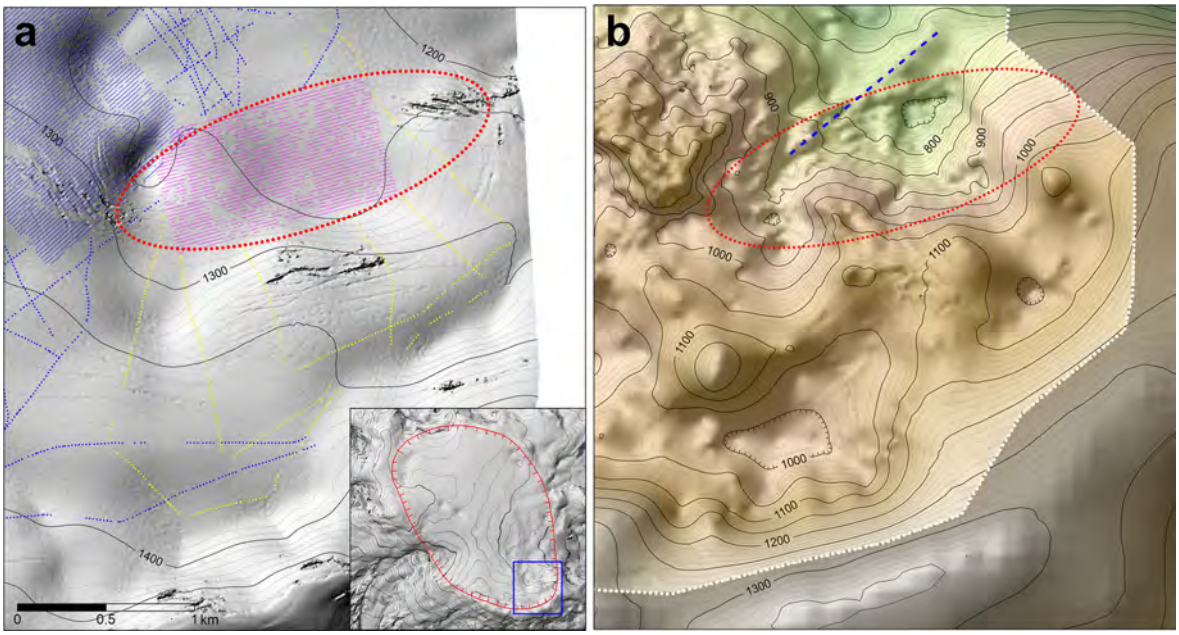

Figure 12. a) The data used for interpolating a new bedrock DEM near the estimated location of the 1918 eruption site (area location within the caldera shown with a blue square on inlet) posted on a surface contour map (10 m contour interval) of September 2019. Blue dotted clusters and lines show locations of RES-data obtained in 2012–2019 (both 2D and 3D migrated). In May 2021, RES-profiles, allowing 3D migration (cluster of magenta dots) as well as 2D migration (yellow dotted lines), were added. b) The resulting bedrock DEM. The area outside the white dotted line, covered with transparent grey mask indicates where bedrock DEM is unchanged from Björnsson *et al.* (2000). The dashed blue line indicates a clear ridge in the bedrock topography at the boundary of the estimated eruption site (Gudmundsson *et al.*, 2021, shown with red dotted ellipse). – *a) Staðsetning íssjármælinga sem nýtt var við gerð botnhæðarkorts af 1918 eldstöðinni (Magnús T. Guðmundsson o.fl., 2021, sýnd með rauðri sporbaugslaga punktalínu) og nágrenni (afmarkað með bláu boxi á innskotsmynd), lagt ofan á yfirborðshæðarkort (10 m hæðarlínubil) frá september 2019. Bláar punktalínur og skellur sýna mælingar frá 2012–2019. Þann 15. maí 2021 var bætt við íssjármælingum sem unnið var úr með þrívíðri (purpurarauðar punktaskellur) og tvívíðri (gular punktalínur) staðsetningarleiðréttingu á endurkastsflötum. b) Nýtt botnhæðarkort (10 hæðarlínubil) af svæðinu. Skyggða svæðið utan hvítu punktalínunnar er óbreytt frá botnkorti Helga Björnssonar o.fl. (2000). Bláa brotalínan gefur til kynna afgerandi hrygg í botnlandslagi í jaðri áætlaðrar gosstöðvar.*

this issue of Jökull. The new survey reveals much more complex topography in this area than the limited RES-data in this area acquired in previous studies (Figure 2). The complex topography is not surprising since most eruptions in the past centuries probably took place within or near this area (Larsen *et al.*, 2013). It is difficult to tell whether any of the observed landforms within this area were formed during the eruption 1918. The most conspicuous form is a ridge aligned from southwest to northeast, partly within the northern part of the suggested eruption area but extending at least 250 m further north. Extended work, beyond the scope of this paper, including comparison with photographs of the eruption site taken by

Kjartan Guðmundsson in June and September 1919 (Gudmundsson *et al.*, 2021) and dense RES-survey spanning the northern end of this ridge may provide further evidences, supporting or rejecting it as a formation of the 1918 eruption. The 2021 survey shows up to 500 m thick ice within the proposed eruption area (in a closed depression south of the aligned ridge in Figure 12b). This is probably less than the maximum thickness at the eruption site in 1918, since the glacier surface was probably a few tens of metres higher than at present. Also, if the eruption left some material at the bed, the current bedrock may also be higher than when the eruption started in 1918. The thick ice at the eruption site and the steep flood route from there (Figure 12) likely facilitated the enormous flow peak of the jökulhlaup (Tómasson, 1996; Larsen *et al.*, 2021) associated with the 1918 eruption.

Acknowledgements

This work was funded by the Icelandic Research fund of Rannís within the project Katla Kalda (project nr. 163391) with further support from The Icelandic Road Administration's Research Fund (project nr. 1800-403). Pléiades images used to produce surface DEMs were acquired at a subsidised cost thanks to the CNES ISIS program. The images used to produce surface DEM in 2019 were further supported through CEOS (Committee on Earth Observation Satellites) contribution to the Iceland Volcanoes Supersite. We thank Hugh Tuffen and an anonymous reviewer for very constructive and detailed reviews, which substantially improved this paper. Magnús T. Guðmundsson, Þórdís Högnadóttir, Guðfinna Aðalgeirsdóttir, Helgi Björnsson, Páll Einarsson, Bryndís Brandsdóttir and Robin E. Bell are thanked for valuable discussions on various aspects of this paper. Sveinbjörn Steinþórsson, Ágúst Þór Gunnlaugsson, Bergur Einarsson, Ásgeir Arnór Stefánsson and Ingibjörg Eiríksdóttir as well as JÖRFÍ volunteers are thanked for their work during field trips.

ÁGRIP

Samspil eldvirkni og jökla og áhrif þess á náttúru og mannlíf hefur óvíða verið meira en í Kötlu í Mýrdalsjökli og nærsveitum hennar. Mýrdalsjökull hefur því allt frá fyrstu tilraunum til ísþykktarmælinga og kortlagningar á botnlandslagi íslenskra jökla verið viðfangsefni slíkra rannsókna. Í fyrstu var beitt bylgjuendurkastsmælingum (Sigurjón Rist, 1967a) en einnig voru þar snemma gerðar tilraunir með íssjá (Helgi Björnsson, 1978). Árið 1991 voru gerðar umfangsmiklar íssjármælingar á jöklinum sem gáfu m.a. upplýsingar um dreifingu, þykkt og rúmmál jökulíssins sem og megindrætti í landslagi Kötluöskjunnar sem er $\sim$100 km^2 að flatarmáli og hulin af hæsta hluta jökulsins (Helgi Björnsson o.fl., 2000). Hér er greint frá ítarlegri íssjármælingum sem gerðar voru á Mýrdalsjökli 2012–2021 með nýrri stafrænni íssjá, sem bæði auðveldar og eykur afkastagetu og nákvæmni við mælingar og úrvinnslu. Auk þess að endurtaka íssjársniðin frá 1991 var þéttleiki mælisniða aukinn á um 116 km^2 svæði sem að mestu leyti er innan öskjurimanna. Í þessari nýju rannsókn var botnlandslag þessa svæðis að stærstum hluta kortlagt eftir samtals $\sim$760 km af íssjársniðum sem unnin voru með tvívíðri staðsetningarleiðréttingu endurkastsflata (e. migration). Á $\sim$14 km^2 svæði í kringum helstu sigkatla Mýrdalsjökuls og áætlaðar gosstöðvar eldgossins 1918 (Magnús T. Guðmundsson o.fl., 2021) voru mæld íssjársnið með einungis 20 m millibili svo að vinna mætti íssjársniðin með þrívíðri staðsetningarleiðréttingu endurkastsflata.

Rannsóknin staðfestir fyrri niðurstöður hvað varðar megindrætti jökulbotns, ísrúmmál innan öskjunnar (45$\pm$2 km^3, haustið 2019) og mestu ísþykkt (740$\pm$40 m). Nýja botnhæðarkortið sýnir hins vegar landslagið undir jöklinum í talsvert meiri smáatriðum, sérstaklega á þéttmældu svæðunum. Landslag megineldstöðvar undir jökli er líklega hvergi eins ítarlega kortlagt eins og á því svæði sem hér er til umfjöllunar. Kortið gefur til kynna flókna og viðburðaríka mótunarsögu fyrir svæðið innan öskjurimanna. Það sýnir m.a. 3–8 km langar raðir hæða og fella, líklega myndað í sprungugosum, fjöll með allt að 250 m háum hamraveggjum sem hafa hlaðist upp í gosum í jökli og djúpar lægðir nærri Goðabungu sem virðast umluktar 100–200 m háum hömrum. Einnig má lesa úr kortinu vísbendingar um að meginaskjan skiptist í fleiri hluta sem gætu tengst fleiri en einum sigatburði. Þetta á sérstaklega við um $\sim$45 km^2 svæði í norðurhluta öskj-

unnar sem er að jafnaði röskum 100 m lægri en aðrir hlutar hennar og afmarkast af norðurbrún meginöskjunnar og stalli í landslagi sem liggur gegnum meginöskjuna miðja frá vestnorðvestri til austsuðausturs.

Hér er einnig gerður samanburður á niðurstöðum botnkortlagningar með íssjá á 2,3 km^2 svæði umhverfis ketil 6, nálægt öskjumiðjunni, þar sem: *a*) ∼200 m voru milli íssjársniða og þau unnin með tvívíðri staðsetningarleiðréttingu endurkastsflata. *b*) 20 m voru milli sniða og þau unnin með þrívíðri staðsetningarleiðréttingu endurkastsflata. Þetta dregur fram takmarkanir þeirra mæli- og úrvinnsluaðferða sem jafnan er beitt og eru sambærilegar við (*a*). Þessar takmarkanir eru hvað mestar yfir fjalllendum jökulbotni en þar má búast við að tvívíð staðsetningarleiðrétting endurkastsflata gefi að jafnaði ofmat í botnhæð sem getur svarað til ∼10 m hæðarhliðrunar.

Vegna betri mælitækni greinast endurköst frá gjóskulaginu sem féll á jökullinn í gosinu 1918 víðar innan öskjunnar í nýju íssjármælingunum en 1991 (Ola Brandt o.fl., 2006). Út frá nýju mælingunum var unnið kort sem sýnir dýpi frá jökulyfirborði niður á gjóskulagið frá 1918 haustið 2016. Einnig er hér birt samskonar dýptarkort af eldra gjóskulagi sem greinist í nyrðri hluta öskjunnar á 420–580 m dýpi. Leiddar eru líkur að því að sú gjóska hafi fallið á jökulinn í einu stærsta Kötlugosi síðasta árþúsunds, árið 1755 (Guðrún Larsen o.fl., 2013). Gjóskulagið frá 1918 er víðast hvar á 200–300 m dýpi. Grynnst er niður á það (∼100 m) yfir vesturrima öskjunnar þar sem líklegt er að skafrenningur dragi úr vetrarsnjósöfnun (Krista Hannesdóttir, 2021). Dýpst er niður á það (∼450 m) í grennd við ketil 6 þar sem verulegur jarðhiti hefur brætt ísinn undan gjóskulaginu, en þar sem áhrif jarðhita eru mest hefur allur jökulís bráðnað undan því og skilið gjóskuna eftir á jökulbotni. Einng má greina í dýptarkorti 1918 gjóskulagsins ummerki áður óþekktra jarðhitasvæða undir Mýrdalsjökli.

REFERENCES

Ágústsson. H., H. Hannesdóttir, Þ. Þorsteinsson, F. Pálsson and B. Oddsson 2013. Mass balance of Mýrdalsjökull ice cap accumulation area and comparison of observed winter balance with simulated precipitation. *Jökull* 63, 9–104.

Belart J. M. C., E. Magnússon, E. Berthier, Á. Þ. Gunnlaugsson, F. Pálsson, G. Aðalgeirsdóttir, T. Jóhannesson, Th. Thorsteinsson and H. Björnsson 2020. Mass balance of 14 Icelandic glaciers, 1945–2017: spatial variations and links with climate. *Front. Earth Sci.* 8(163). https://doi.org/10.3389/feart.2020.00163.

Björnsson, H. 1975. Subglacial water reservoirs, jökulhlaups and volcanic eruptions. *Jökull* 25, 1–15.

Björnsson H. 1978. Könnun á jöklum með rafsegulbylgjum. *Náttúrufræðingurinn* 47 (3–4), 184–194.

Björnsson, H. 2010. Understanding jökulhlaups: from tale to theory. *J. Glaciol.* 56(200), 1002–1010. https://doi.org/10.3189/002214311796406086.

Björnsson, H. 2017. The glaciers of Iceland. A historical, cultural and scientific overview. *Atlantis Advances Quat. Sci.*, Atlantis Press, ISBN 978-94-6239-206-9.

Björnsson, H. and F. Pálsson 2020. Radio-echo soundings on Icelandic temperate glaciers: History of techniques and findings. *Ann. Glaciol.* 61(81), 25–34. https://doi.org:/10.1017/aog.2020.10.

Björnsson H, F. Pálsson and M. T. Gudmundsson 2000. Surface and bedrock topography of Mýrdalsjökull, Iceland: The Katla caldera, eruption sites and routes of jökulhlaups. *Jökull* 49, 29–46.

Brandt, O., H. Björnsson and Y. Gjessing 2006. Mass-balance rates derived by mapping internal tephra layers in Mýrdalsjökull and Vatnajökull ice caps, Iceland. *Ann. Glaciol.* 42, 284–290. https://doi.org/10.1017/aog.2020.10.

Cuffey, K. M. and W. S. B. Paterson 2010. The Physics of Glaciers. Academic Press, Burlington, MA, 4th edn., 704 pp., ISBN: 978-0-123-69461-4.

Dadic, R., R. Mott, M. Lehning and P. Burlando 2010. Wind influence on snow depth distribution and accumulation over glaciers. *J. Geophys. Res.* 115, F01012. https://doi.org/10.1029/2009JF001261.

Einarsson, B. 2019. Samantekt um jökulhlaup og ummerki leka frá jarðhitakötlum í Mýrdalsjökli 2010–2018 í gögnum úr vöktunarmælum í Markarfljóti, Múlakvísl og Jökulsá á Sólheimasandi. Tech. Report: BE/2019-01, Icelandic Meteorological Office.

Elíasson, J., G. Larsen, M. T. Guðmundsson and F. Sigmundsson 2005. Líkindi eldgosa, hlaupa og færslu eldvirkni milli svæða innan Kötluöskjunnar. In: Guðmundsson, M. T. and Á. G. Gylfason (eds.). *Hættumat vegna eldgosa og hlaupa frá vestanverðum Mýrdalsjökli og Eyjafjallajökli.* Ríkislögreglustjórinn/Háskólaútgáfan, Reykjavík, 135–150.

Elíasson, J., G. Larsen, M. T. Gudmundsson and F. Sigmundsson 2006. Probabilistic model for eruptions and associated flood events in the Katla caldera, Iceland. *Computational Geosciences* 10, 179–200. https://doi.org/10.1007/s10596-005-9018-y.

Eyþórsson, J. 1945. Um Kötlugjá og Mýdalsjökul. *Náttúrufræðingurinn* 15, 145–174.

Fürst, J. J., F. Gillet-Chaulet, T. J. Benham, J. A. Dowdeswell, M. Grabiec, F. Navarro, R. Pettersson, G. Moholdt, C. Nuth, B. Sass, K. Aas, X. Fettweis, C. Lang, T. Seehaus and M. Braun 2017. Application of a two-step approach for mapping ice thickness to various glacier types on Svalbard. *The Cryosphere* 11, 2003–2032. https://doi.org/10.5194/tc-11-2003-2017.

Galeczka, I., E. Oelkers and S. Gislason 2014. The chemistry and element fluxes of the July 2011 Múlakvísl and Kaldakvísl glacial floods, Iceland. *J. Volc. Geoth. Res.* https://doi.org:/273.10.1016/-j.jvolgeores.2013.12.004.

Glen, J. W. 1955. The creep of polycrystalline ice. *Proceedings of the Royal Society of London A: Math. Phys. Eng. Sci.* 228, 519–538. https://doi.org/-10.1098/rspa.1955.0066.

Guðmundsson M. T. 2000. Mass balance and precipitation on the summit plateau of Öræfajökull, SE-Iceland. *Jökull* 48, 49–54.

Guðmundsson, Ó., B. Brandsdóttir, W. H. Menke and G. E. Sigvaldason 1994. The crustal magma chamber of the Katla volcano in south Iceland revealed by seismic undershooting. *Geophys. J. Int.* 119, 277–296. https://doi.org/10.1111/j.1365-246X.1994.tb00928.x.

Gudmundsson, M. T. and Þ. Högnadóttir 1999–2020. http://earthice.hi.is/monitoring_ice_cauldrons.

Guðmundsson, M. T., J. Elíasson, G. Larsen, Á. G. Gylfason, P. Einvarsson, T. Jóhannesson, K. M. Hákonardóttir and H. Torfason 2005a. Yfirlit um hættu vegna eldgosa og hlaupa frá vesturhluta Mýrdalsjökuls og Eyjafjallajökli. In: Guðmundsson, M. T. and Á. G. Gylfason (eds.). *Hættumat vegna eldgosa og hlaupa frá vestanverðum Mýrdalsjökli og Eyjafjallajökli.* Ríkislögreglustjórinn/Háskólaútgáfan, Reykjavík, 11–44.

Guðmundsson M. T. and Þ. Högnadóttir 2005b. Ísbráðnun og upptakarennsli jökulhlaupa vegna eldgosa í Eyjafjallajökli og vestanverðum Mýrdalsjökli. In: Guðmundsson, M. T. and Á. G. Gylfason (eds.). *Hættumat vegna eldgosa og hlaupa frá vestanverðum Mýrdalsjökli og Eyjafjallajökli.* Ríkislögreglustjórinn/Háskólaútgáfan, Reykjavík, 159–180.

Gudmundsson, M. T., Th. Högnadóttir, A. B. Kristinsson and S. Guðbjörnsson 2007. Geothermal activity in the subglacial Katla caldera, Iceland, 1999–2005, studied with radar altimetry. *Ann. Glaciol.* 45, 66–72. https://doi.org/10.3189/172756407782282444.

Gudmundsson, M. T., G. Larsen, Á. Höskuldsson and Á. G. Gylfason 2008. Volcanic hazards in Iceland. *Jökull* 58, 251–268.

Guðmundsson, M. T. and Þ. Högnadóttir 2011. *Upptök og stærð jökulhlaups í Múlakvísl – niðurstöður flugmælinga.* Memo written 13 July, 2011.

Guðmundsson M. T. and G. Larsen 2013. Jökulhlaup. In: Sólnes, J., F. Sigmundsson and B. Bessason (eds.). *Náttúruvá á Íslandi.* Viðlagatrygging Íslands/Háskólaútgáfan, Reykjavík, 156–170, ISBN: 978-9979-54-943-7.

Gudmundsson, M. T., M. H. Janebo, G. Larsen, Þ. Högnadóttir, T. Thordarson, J. Gudnason and T. Jónsdóttir 2021. The explosive, basaltic Katla eruption in 1918, south Iceland: II. Isopach map, ice cap deposition of tephra and layer volume. *Jökull* 71, 21–38. https://doi.org/10.33799/jokull2021.71.021

Hannesdóttir K. 2021. *Estimating snow accumulation on Mýrdalsjökull and Öræfajökull with snow radar using Discrete Gabor Transform for image analysis. Implications to the mass balance of ice cauldrons.* M.Sc-thesis, Faculty of Earth Sciences, University of Iceland, 170 pp.

Ilyinskaya, E., S. Mobbs, R. Burton, M. Burton, F. Pardini, M. A. Pfeffer, R. Purvis, J. Lee, S. Bauguitte, B. Brooks, I. Colfescu, G. N. Petersen, A. Wellpott and B. Bergsson 2018. Globally significant CO_2 emissions from Katla, a subglacial volcano in Iceland. *Geophys. Res. Lett.* 45, 10,332– 10,341. https://doi.org/-10.1029/2018GL079096.

Jarosch, A. H. 2008. Icetools: A full Stokes finite element model for glaciers. *Computers and Geosciences* 34, 1005–1014. https://doi.org/10.1016/-j.cageo.2007.06.012.

Jarosch, A. H., E. Magnússon, A. Wirbel, J. M. C. Belart and F. Pálsson 2020. *The geothermal output of the Katla caldera estimated using DEM differencing and 3D-iceflow modelling.* Report: RH-02-20. https://doi.org/10.5281/zenodo.3784657.

Jóhannesson, T. 2012. Jökulhlaup í Múlakvísl 9. júlí 2011. *Sigkatlar í Mýrdalsjökli mældir með leysimælingu úr flugvél.* Tech. Report: ToJ/2012-01, Icelandic Meteorological Office.

Jóhannesson, T., H. Björnsson, E. Magnússon, S. Guðmundsson, F. Pálsson, O. Sigurðsson, T. Thorsteinsson and E. Berthier 2013. Ice-volume changes, bias-estimation of mass-balance measurements and changes in subglacial water bodies derived by lidar mapping of the surface of Icelandic glaciers. *Ann. Glaciol.* 54(63), 63–74. https://doi.org/10.3189/2013AoG63A422.

Jóhannesson, T., B. Pálmason, Á. Hjartarson, A. H. Jarosch, E. Magnússon, J. M. C. Belart and M. T. Gudmundsson 2020. Non-surface mass balance of glaciers in Iceland. *J. Glaciol.* 66(258), 685–697. https://doi.org/10.1017/jog.2020.37.

Jónsson, G. Þ. and T. Þórarinsdóttir 2011. *Hlaup í Múlakvísl 8.–10. júlí 2011.* Tech. Report: GThJ-TTh/2011-01. Icelandic Meteorological Office, 10 pp.

Lapazaran, J. J., J. Otero, A. Martín-Español and F. J. Navarro 2016. On the errors involved in ice-thickness estimates I: ground-penetrating radar measurement errors. *J. Glaciol.* 62(235), 1–13. https://doi.org/10.1017/jog.2016.93.

Larsen, G. 2000. Holocene eruptions within the Katla volcanic system, south Iceland: Characteristics and environmental impact. *Jökull* 49, 1–28.

Larsen, G. 2010. Katla: Tephrochronology and eruption history. In: Schomacker, A., J. Krüger and K. Kjær (eds.). The Mýrdalsjökull ice cap, Iceland: glacial processes, sediments and landforms on an active volcano. *Development in Quaternary Sci.* 13, 23–49. Elsevier, Amsterdam, ISBAN: 978-0-444-53045-5.

Larsen, G., M. T. Guðmundsson and O. Sigmarsson 2013. Sólnes, J., F. Sigmundsson and B. Bessason (eds.). *Náttúruvá á Íslandi.* Viðlagatrygging Íslands/Háskólaútgáfan, Reykjavík, 211–233, ISBN: 978-9979-54-943-7.

Larsen, G. and Þ. Högnadóttir 2021. Ljósmyndir Þorláks Sverrissonar í Vík: Kötlugosið 1918 í nýju ljósi. *Jökull* 71, 95–114. https://doi.org/10.33799/jokull2021.71.095

Larsen, G., M. H. Janebo and M. T. Gudmundsson 2021. The explosive basaltic Katla eruption in 1918, south Iceland I: Course of events, tephra fall and flood routes. *Jökull* 71, 1–20. https://doi.org/10.33799/jokull2021.71.001

Mackintosh, A. N., A. J. Dugmore and F. M. Jacobsen 2000. Ice-thickness measurements on Sólheimajökull, southern Iceland, and their relevance to its recent behaviour. *Jökull* 48, 9–15.

Magnússon, E., J. M.-C. Belart, F. Pálsson, L. S. Anderson, Á. Þ. Gunnlaugsson, E. Berthier, H. Ágústsson and Á. Geirsdóttir 2016. The subglacial topography of Drangajökull ice cap, NW-Iceland, deduced from dense RES-profiling. *Jökull* 66, 1–26.

Magnússon, E., F. Pálsson, H. Björnsson and S. Guðmundsson 2012. Removing the ice cap of Öræfajökull central volcano, SE-Iceland: Mapping and interpretation of bedrock topography, ice volumes, subglacial troughs and implications for hazards assessments. *Jökull* 62, 131–150.

Magnússon, E., F. Pálsson, M. T. Guðmundsson, J. M. C. Belart and Þ. Högnadóttir 2017. *Hvað sýna íssjármælingar undir sigkötlum Mýrdalsjökuls.* Tech. report: Institute of Earth Sciences, University of Iceland, 39 pp.

Magnússon, E., F. Pálsson, M. T. Gudmundsson, Th. Högnadóttir, C. Rossi, B. G. Ófeigsson, Th. Thorsteinsson, E. Sturkell and T. Jóhannesson 2021.Development of a subglacial lake monitored with radio-echo sounding: case study from the eastern Skaftá cauldron in the Vatnajökull ice cap, Iceland. *The Cryosphere* 15, 3731–3749. https://doi.org/10.5194/tc-15-3731-2021.

Mingo, L. and G. E. Flowers 2010. Instruments and Methods. An integrated lightweight ice-penetrating radar system. *J. Glaciol.* 56(198), 709–714. https://doi.org/10.3189/002214310793146179.

Moran, M. L., R. J. Greenfield, S. A. Arcone and A. J. Delaney 2000. Delineation of a complexly dipping temperate glacier bed using short-pulse radar arrays. *J. Glaciol.* 46(153), 274–286. https://doi.org/10.3189/172756500781832882.

Morlighem, M., E. Rignot , H. Seroussi, E. Larour, H. Ben Dhia and D. Aubry 2011. A mass conservation approach for mapping glacier ice thickness. *Geophys. Res. Lett.* 38, L19503. https://doi.org/10.1029/2011GL048659

Óladóttir, B. A., G. Larsen and O. Sigmarsson 2014. Volume estimates of nine Katla tephra layers (∼1860 BC – 870 AD). *Jökull* 64, 23–40.

Óladóttir, B. A., O. Sigmarsson, G. Larsen and T. Thordarson 2008. Katla volcano, Iceland: magma composition, dynamics and eruption frequency as recorded by Holocene tephra layers. *Bull. Volc.* 70 (4), 475–493. https://doi.org/10.1007/s00445-007-0150-5.

Pálsson F., H. Björnsson and E. Magnússon 2005. *Rennslisleiðir vatns undir Kötlujökli (Höfðabrekkujökli).* Report, RH-04-2005.

Rist, S. 1967a. The thickness of the ice cover of Mýrdalsjökull, Southern Iceland. *Jökull* 17, 237–242.

Rist, S. 1967b. Jökulhlaups from the ice cover of Mýrdalsjökull on June 25, 1955 and January 20, 1956. *Jökull* 17, 243–248.

Rist, S. and S. Þórarinsson 1955. Rannsókn á Kötlu og Kötluhlaupi sumarið 1955. *Jökull* 5, 43–46.

Russell, A. J., F. S. Tweed, M. J. Roberts, F. D. Harris, M. T. Gudmundsson, Ó. Knudsen and P. M. Marren 2010. An unusal jökulhlaup resulting from subglacial volcanism, Sólheimajökull, Iceland. *Quat. Sci. Rev.* 29, 1363–1381. https://doi.org/10.1016/j.quascirev.-2010.02.023.

Schlegel, R., A. Booth, T. Murray, A. Smith, A. Brisbourne, E. King, R. Clark and S. Cornford 2020. *3D imaging of subglacial lineations under the Rutford Ice Stream, West Antarctica.* EGU General Assembly 2020, Online, 4–8 May 2020, EGU2020-7644. https://doi.org/10.5194/egusphere-egu2020-7644.

Schneider, W. A. 1978. Integral formulation for migration in two and three dimensions. *Geophysics* 43, 49–76. https://doi.org/10.1190/1.1440828.

Sgattoni, G., F. Lucchi, P. Einarsson, Ó. Gudmundsson, G. D. Astis and C. A. Tranne 2019. The 2011 unrest at Katla volcano: seismicity and geology context. *Jökull* 69, 53–70.

Sigbjarnason, G. 1973. Katla and Askja. *Jökull* 23, 45–50.

Sigurðsson, O., S. Zóphóníasson and E. Ísleifsson 2000. Jökulhlaup úr Sólheimajökli 18. júlí 1999. *Jökull* 49, 75–80.

Smith, K. and H. Haraldsson 2005. A late Holocene jökulhlaup, Markarfljót, Iceland: nature and impacts. *Jökull* 55, 75–86.

Sverrisson, M., Æ. Jóhannesson and H. Björnsson 1980. A radio-echo equipment for depth sounding of temperate glaciers. *J. Glaciol.* 25(93), 477–486. https://doi.org/10.3189/S0022143000015318.

Thorarinsson, S. 1957. The jökulhlaup from the Katla area in 1955 compared with other jökulhlaups in Iceland. *Jökull* 7, 21–25.

Tómasson, H. 1996. Jökulhlaup from Katla in 1918. *Ann. Glaciol.* 22, 249–254. https://doi.org/10.3189/-1996AoG22-1-249-254.

Tryggvason, E. 1960. Earthquakes, jökulhlaups and subglacial eruptions. *Jökull* 10, 18–22.

Þórarinsson, S. 1975. Katla og annáll Kötlugosa (Katla and annals of Kötlu eruptions). *Árbók Ferðafélags Íslands*, Reykjavík, 125–149.